Active Thermal Augmentation and Ultra Dense MEMS-Based Electrospray Thrusters

by

Matthew Nicholas Corrado

B.S., Georgia Institute of Technology (2020)

Submitted to the Department of Aeronautics and Astronautics
in partial fulfillment of the requirements for the degree of

Master of Science in Aeronautics and Astronautics

at the

MASSACHUSETTS INSTITUTE OF TECHNOLOGY

May 2022

Author .....
Department of Aeronautics and Astronautics
May 17, 2022

Certified by .....
Paulo C. Lozano
M. Alemán-Velasco Professor of Aeronautics and Astronautics
Thesis Supervisor

Accepted by .....
Jonathan P. How
R. C. Maclaurin Professor of Aeronautics and Astronautics
Chair, Graduate Program Committee

Active Thermal Augmentation and Ultra Dense MEMS-Based Electrospray Thrusters

by

Matthew Nicholas Corrado

Submitted to the Department of Aeronautics and Astronautics
on May 17, 2022, in partial fulfillment of the
requirements for the degree of
Master of Science in Aeronautics and Astronautics

Abstract

Ionic liquid electrospray thrusters, a highly efficient form of electric space propulsion, have several advantages over traditional chemical forms of space propulsion as well as competing forms of electric propulsion, including their unique scalability down to extremely small sizes, their use of nontoxic propellants that do not require special storage or pressurization, and their ability to be operated in a bipolar mode, eliminating the need for bulky and complex neutralizers. Electrosprays still lag behind other forms of electric propulsion, such as Hall Effect Thrusters and Gridded Ion Engines, in thrust density, a key figure of merit for propulsion systems intended for small spacecraft that have limited surface area available for propulsion systems. A path forward to ultimately improve electrospray thrust density is proposed, and proofs of concept are tested. Increasing thrust density requires accomplishment of at least one of two feats: increasing the number of ion emission sites per unit area, or increasing the magnitude of current capable of being extracted per emission site. Advances in microelectromechanical systems (MEMS) fabrication techniques have enabled the former, and an ultra-dense silicon-based ionic liquid electrospray thruster with record-breaking emitter density is tested. The densified electrospray thruster is successfully fired, exhibiting emission in the pure ionic regime and performance characteristics comparable to the state of the art. The latter can be achieved by thermally augmenting the current output of an electrospray thruster, leveraging the temperature dependence of propellant properties and fluid mechanics of propellant transport. The applications of such a system are discussed and analyzed, and a prototype for a thermally augmented electrospray thruster is designed and tested, verifying the concept of current augmentation at elevated temperatures.

Thesis Supervisor: Paulo C. Lozano
Title: M. Alemán-Velasco Professor of Aeronautics and Astronautics

Acknowledgments

This material is based upon work supported by the National Science Foundation Graduate Research Fellowship Program. Thank you to the NSF for its support.

First, thank you to my advisor, Dr. Paulo Lozano, for your dedication to your students. Starting grad school during a pandemic was not always easy, but your mentorship made it significantly easier, and your trust in me as a researcher allowed me to find my footing despite the chaos. Thank you to my fellow grad students in the SPL who, incredibly, sit and willingly listen to my endless rants and somehow make me laugh once I'm done. Thank you to the team at MIT Lincoln Lab for affording me the privilege of working on this research and for trusting me and my judgement. Most importantly, thank you to my family for your truly unwavering support and love. Sam, thank you for inspiring me to study engineering and always holding me accountable. Ben, thank you for showing me your work ethic and for spending hours talking baseball with me. Mom and Dad, there isn't anything I can say to sufficiently express my deep appreciation for all that you do for us. You stop at absolutely nothing to ensure that your children are as happy and comfortable as possible, and I am incredibly proud to be your son. It is with great gratification and some relief that I reach this milestone, and many more thanks are deserved to many more people who have helped me along the way. I say with confidence that both the best and worst moments of my life (so far...) have occurred during these past two years while I've been a student at MIT. As I prepare to spend several more years at this institution in pursuit of a PhD, I can only hope for more bests and fewer worsts.

Contents

List of Figures

List of Tables

Chapter 1

Introduction

1.1 Historical Perspective

While the concept of expelling matter from a device to increase its velocity has been in use for millennia, the study of rocketry as a science is typically traced back to the work of Konstantin Tsiolkovsky, who in 1903 published his “Investigation of Universal Space by Means of Reactive Devices" [69] and envisioned propulsive devices that could function in a vacuum, thus birthing the field of space propulsion [7]. In this visionary work, Tsiolkovsky derived what became known as the Ideal Rocket Equation, which he originally wrote in the form

$$\frac{\Delta v}{v_e} = \ln(1 + \frac{m_p}{m_s}) \tag{1.1}$$

where Δv is the change in velocity of the rocket, v_e is the exhaust velocity of the ejected material, m_p is the initial mass of propellants, and m_s is the structural mass, or the initial mass of the rocket excluding the propellants. With Tsiolkovsky assuming that in his derivation of equation 1.1 that all the propellant mass is consumed to achieve the Δv, we can easily rearrange the equation into its more common and more general form

$$\Delta v = v_e \ln(\frac{m_0}{m_f}) \tag{1.2}$$

where m_0 and m_f are the initial and final total mass, respectively.

Only 8 years later, in a sequel to his 1903 article, did Tsiolkovsky first mention the possibility of using electricity to accelerate particles of lower mass than combustion products to extremely high velocities, using cathode ray tubes as an example [69]. While no practical electric propulsion device today relies on electron momentum due to their extremely low mass and correspondingly negligible thrust, Tsiolkovsky correctly predicted in 1911 the use of electric fields to accelerate charged particles away from a spacecraft to produce thrust. After a more formal scientific understanding of positively charged particles was established in the first quarter of the 20th century, positive or negative ions rather than electrons were targeted as preferable exhaust products so that meaningful thrust can be produced while the achievable exhaust velocities are still orders of magnitude larger than those for combustion products.

Despite a relatively early understanding of the concept of EP, it would be another half century before the first electric thruster, an electrostatic ion engine, took flight on the SERT I mission carried out by NASA in 1964 [28]. Since this first ballistic test flight, at least several hundred spacecraft utilizing some type of EP have been launched into Earth orbit and beyond [61], and with the emergence of megaconstellations of small satellites using EP, hundreds to thousands more electric thrusters per year may be launched in the coming decade.

1.2 Electric Propulsion

Electric propulsion technology can be divided into three main categories based on the fundamental method of ion acceleration [54]:

1. Electrostatic: Electrical power is used to ionize a neutral propellant, and charged particles in the plasma are accelerated by a static electric field.

2. Electrothermal: Electrical power is used to heat a neutral propellant, and the neutral substance with increased enthalpy is expanded through a nozzle.

3. Electromagnetic: Electrical power is used to ionize a neutral propellant, and

the plasma is accelerated by the combined action of an electric and magnetic field (the Lorentz force).

Each type of EP can be further divided into several distinct technologies that apply the same acceleration mechanism in a fundamentally unique manner. However, the intricate details of each type of EP will not be discussed here. Instead, we shift our focus to electrostatic thrusters, which have the most in-space heritage. In an electrostatic thruster, propellants are typically stored as neutral substances. Various applications of electrostatic thrusters have used gases, liquids, and solids as propellants. Common gaseous propellants include the heavy noble gases like Xenon and Krypton for their chemical inertness, large atomic mass, high storage density (compared to other gases), and relatively low ionization energy. Propellants that can be stored as solids are advantageous due to their extremely high storage density and their lack of need for pressurized tanks. These solid propellants are typically melted (in the case of metals like Cesium or Indium) or vaporized (in the case of novel propellants like Iodine or Teflon) prior to being ionized, which comes at a power penalty. Liquid propellants carry most of the advantages of solids, including high storage density and lack of pressurization, but without some of the disadvantages like the need to change phase prior to injection.

Electrospray thrusters, a type of electrostatic thruster, take advantage of the properties of liquid propellants, specifically room temperature ionic liquids (RTILs), to pack massive capability into extremely small volumes, making them one of the most mass- and volume-efficient forms of EP. The following sections will review in detail the mechanisms by which electrosprays function and the state of the art in the technology.

First, we examine the mechanism by which electric thrusters, or any type of rocket propulsion, exert forces on vehicles. For this, we take a closer look at the derivation of Tsiolkovsky's rocket equation (1.1). Consider a vehicle with instantaneous mass m moving with velocity v in an inertial reference frame. The vehicle is ejecting mass with relative exhaust velocity c at a rate $\dot{m}$. The total momentum of the system in the inertial frame, P_m, is

$$P_m = mv + \int_0^t \dot{m}(v(\tau) - c)d\tau \tag{1.3}$$

where the integral on the right hand side represents the cumulative momentum of the exhaust at time t. For a closed system in an inertial reference frame, momentum must be constant, so,

$$\frac{dP_m}{dt} = 0 = m\frac{dv}{dt} + v\frac{dm}{dt} + \dot{m}(v - c) \tag{1.4}$$

Note that the rate of change of the vehicle mass, dm/dt, is equal and opposite to the rate at which exhaust accumulates: $dm/dt = -\dot{m}$. Thus,

$$m\frac{dv}{dt} - v\dot{m} + \dot{m}v - \dot{m}c = m\frac{dv}{dt} - \dot{m}c = 0 \tag{1.5}$$

The term mdv/dt in equation 1.5 is the instantaneous mass of the vehicle multiplied by its instantaneous acceleration, which is equal to the force on the vehicle due to the exhaust, so in a vacuum the thrust of a rocket engine operating with flow rate $\dot{m}$ and exhaust velocity c can be written as,

$$F = \dot{m}c \tag{1.6}$$

Equation 1.6 is an important result in the field of space propulsion, as it reveals that without any forces except for that due to the momentum exchange between the vehicle and the exhaust, the force on the vehicle is proportional to both the mass flow rate and relative velocity of the expelled material.

1.3 Electrospray Propulsion

Electrospray thrusters, like all other types of electric propulsion, produce thrust by converting electrical energy to kinetic energy of exhaust particles. In the case of electrosprays, charged particles are accelerated to high velocity by a large electric field induced by application of a potential difference between an emitter and downstream

extractor electrode, as shown in Figure 1-1. The extractor electrode contains apertures directly in front of the ion emission sites to allow for the ion beam to leave the system as exhaust and produce thrust.

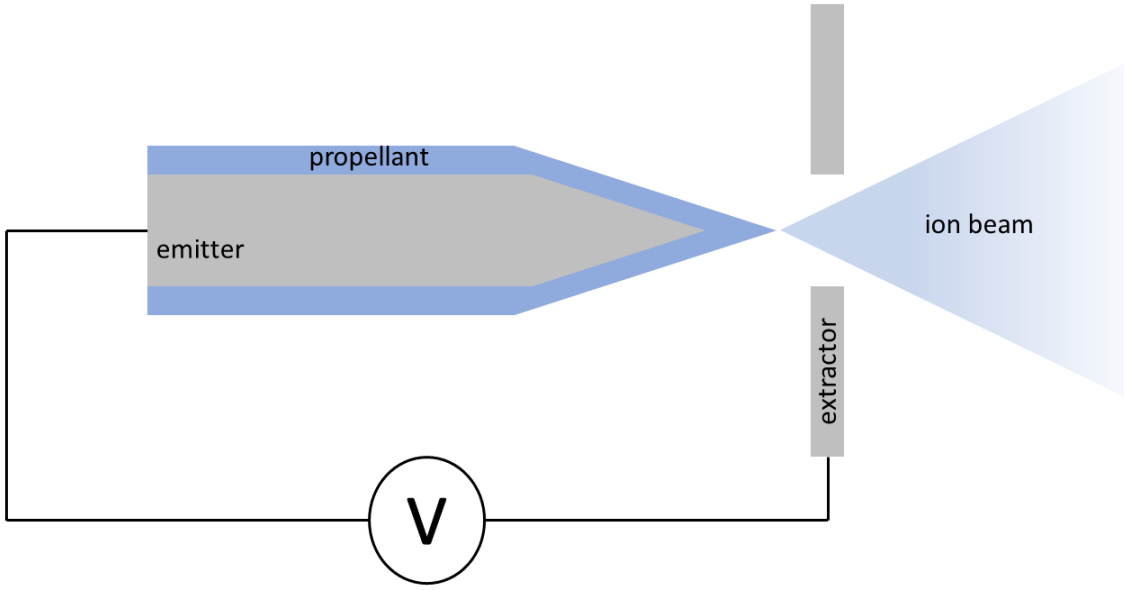

Figure 1-1: Conceptual schematic of a single electrospray emitter tip.

Under the influence of an electric field induced by biasing the propellant on the emitter electrode relative to the extractor, ions accumulate on the liquid interface and strain the surface to form a near-conical meniscus, the geometry of which balances electric stress and surface tension at equilibrium [43]. The equilibrium geometry is known as a Taylor cone, named for Geoffrey Taylor who derived the universal equilibrium angle $\theta_T = 49.29°$ and confirmed it experimentally in 1964 [68].

Several architectures for electrospray thrusters have been studied and implemented. Some of the first electrosprays fed conductive liquid propellant though small hollow capillaries biased to high potentials, causing the liquid at the tip of the capillaries to form a meniscus whose shape approaches a Taylor cone and disintegrates into nanoscopic charged droplets [9]. The most common propellant was glycerol doped with sodium iodide. These thrusters are commonly referred to as a colloid thrusters.

Eventually, ionic liquids were investigated for use as propellants in colloid thrusters.

Ionic liquids are room temperature molten salts that have many benefits as electrospray propellants, including but not limited to their tendency to remain liquid at relatively low temperatures, their negligible vapor pressure which prevents loss of mass due to evaporation in vacuum, and their high conductivity relative to the glycerol-based solutions that preceded them. Work at MIT and elsewhere popularized the use of ionic liquids in electrosprays, especially as the ability to create beams composed of pure ions was studied and characterized [42].

Electrospray emission exists in three regimes: At relatively large flowrates, the singularity near the apex of the Taylor cone breaks down into a jet that separates into nanoscopic charged liquid droplets. Reduction of the flowrate causes the electric field near the surface of the jet to approach the a critical threshold above which field evaporation starts to occur [39], and the emission enters a regime characterized by a mixture of ions and charged droplets. As flowrate is decreased further, the liquid jet becomes unstable, and only pure ions are emitted from the cone surface [8]. The latter mode is known as the pure-ion regime (PIR).

Operation in the PIR is attractive for space propulsion applications because the high charge-to-mass ratio, q/m, of the ions compared to droplets affords large exhaust velocities and therefore high specific impulse. Ion emission from ionic liquids is often modeled as an activated process [43] in which there exists an energy barrier for ion evaporation (also called the solvation energy), ΔG, which can be related to the critical electric field E^*, which scales as,

$$E^* = \frac{4\pi\varepsilon_0}{e}\Delta G^2 \tag{1.7}$$

The solvation energy for ionic liquids is approximately 1.2 eV, which results in a critical electric field on the order of 1-2 $\mathrm{V\,nm^{-1}}$ [60]. Field of such magnitude are possible when a conductive liquid meniscus deforms under electric stress. By balancing the electric pressure against surface tension, it is possible to estimate the curvature length scale required to reach E^*.

$$\frac{1}{2}\varepsilon_0 E^{*2} = 2\frac{\gamma}{r^*} \tag{1.8}$$

Evaluating equation 1.8 with $\gamma \approx 0.05$ N m (typical for many common ionic liquids) reveals that the scale of the site on which ion evaporation occurs is $r^* \approx 10$ nm. Due to the extremely small scale of r^*, large numbers of microscopic emission sites firing in parallel can be grouped together to increase the total current emitted from a single macroscopic device.

The electric field at the surface of a tip with radius of curvature R_c and flat extraction electrode at distance d from the emitter apex can be estimated by considering the potential field in prolate spheroidal coordinates. The approximation is given in equation 1.9. This analysis does not consider space charge or applied pressures, and it assumes a confocal hyperboloid geometry of the emitting meniscus. As such, the estimate for E_{tip} and the subsequent estimate for V_{start} serve as order of magnitude approximations rather than exact values.

$$E_{tip} \approx -\frac{2V/R_c}{\ln\left(4d/R_c\right)} \tag{1.9}$$

Combining equations 1.8 and 1.9 and rearranging variables gives an approximation for V_{start} based on geometric parameters and fluid properties,

$$V_{start} \approx \sqrt{\frac{\gamma R_c}{\varepsilon_0}} \ln\left(\frac{4d}{R_c}\right) \tag{1.10}$$

1.3.1 The ion Electrospray Propulsion System

The state of the art in electropray propulsion is the ion Electrospray Propulsion System (iEPS) developed in the Space Propulsion Laboratory (SPL) at MIT. The iEPS is a cubesat-scale propulsion system based on ionic liquid electrospray technology. Microelectromechanical systems (MEMS) manufacturing techniques are used to etch hundreds of microscopic emitter tips into a porous glass substrate, through which ionic liquid propellant is transported from an external reservoir to the apex of the tips.

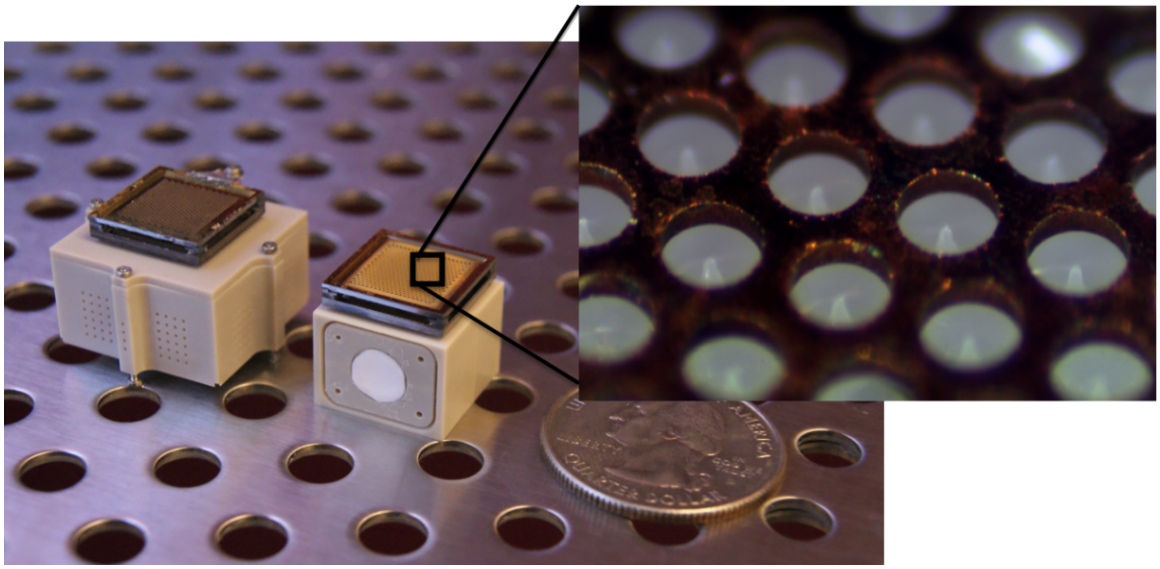

Figure 1-2: Two generation of iEPS tank designs with thruster chips mounted on top

The use of porous, passively-fed emitters is now commonplace in the field of electrospray propulsion, but optimization of ionic liquid electrosprays is still the subject of ongoing research for several space propulsion research groups and commercial ventures. Electrospray thrusters compete with technologies such as Hall Effect Thrusters (HETs) and Gridded Ion Engines (GIEs), which have both seen an increase in reliability and flight heritage over the last several decades. However, a class of increasingly small yet capable satellites demands a novel and miniaturized approach to electric propulsion, and addressing some of the limitations of electrospray thrusters will make them a more technically attractive option for such systems, many of which require extremely small and agile technology to perform complex and coordinated maneuvers.

1.3.2 Limitations

Several limitations in the state of the art of electrosprays have limited their widespread adoption as in-space propulsion. Of primary importance is thruster lifetime [4, 5, 30, 31, 35]. An iEPS thruster has been fired continuously for up to 172 hours [35], but they more commonly operate for 80-100 hours before one of several lime-limiting mechanisms renders them unusable. Examples of such mechanisms include the development of a short circuit between the emitter and extractor brought on by discharges

between the closely-spaced electrodes, electrochemical wear on the emitter tips and/or inside the propellant reservoir resulting in degradation of tip geometry or excessive loss of propellant to reduction-oxidation reactions, and ion impingement leading to propellant accumulation on the extractor grid.

Mitigation techniques for each of the life-limiting mechanisms have been engineered. For instance, electrochemical degradation occurs when a thruster emits an ion beam of a single polarity, leaving excess of the counterion in the liquid near the surface of the emitting tip. This lack of neutrality causes the formation of an electrical double layer at the liquid-surface interface, and after the charge stored exceeds a materially-dependent threshold, an electron is transferred between the liquid and solid surfaces, known as an electrochemical reaction. These reactions release energy into the small volume near the emission site, leading to wear and sometimes total degradation of the tip, and the resultant products of these reactions can be undesriable or even dangerous. To mitigate these electrochemical reactions, a distal electrode is introduced to simultaneously force the site of any electrochemical reactions to the surface of the electrode itself rather than at the apex of the emitter tips, and extend the time scale over which the electrical double layer forms to allow for complete avoidance of electrochemistry if the applied potential can be alternated at a sufficient frequency [4].

To mitigate effects related to shorting of the thruster circuit and propellant accumulation, care is taken in the design of electrospray thrusters to control the flow of the ionic liquid propellant and the trajectory of the expelled ions beams. For instance, physical and thermodynamic barriers are implemented to prevent propellant creep from the emitter electrode to the extractor electrode. In addition, thin hydrophobic coatings are used to prevent excess propellant accumulation on the emitter surface, which can cause short circuits. Finally, emitter tips fabricated with precise geometries and wide extractor apertures are used to ensure that the ion beam is emitted in the intended direction and can travel through the extractor while spreading without impinging on the extractor grid.

After firing for long durations, the probability of at least one of the mechanisms

above causing total failure of the thruster increases dramatically, so several research groups are working on solutions that will lengthen the lives of electrospray thrusters, thus enabling their use on long-duration space missions.

Of secondary importance is the performance of electrospray thrusters. Electrosprays compete well with other forms of EP in several figures of merit, including specific impulse and thrust efficiency. Electrosprays also benefit from their ability to be scaled down to sizes much smaller than the conventional forms of EP such as HETs and GIEs. Electrosprays are scalable because the physical phenomena driving ion emission occur on the nanometer scale, the propellant is "pre-ionized" in that no volume is required for ionization as is the case with noble gas propellants, and heat generation is negligible, removing concerns related heat dissipation as the ratio of surface area to volume decreases.

Despite the benefits of electrosprays, they lag behind competing forms of EP in thrust density, or thrust per unit area. Thrust density is an important figure of merit for satellite engineers because surface area on small satellites is typically limited, and it is desired to maximize the area available for scientific payloads. Typical thrust densities of the most common forms of EP range on the order of 1-5 $\mathrm{N\,m^{-2}}$ for GIEs and 10-30 $\mathrm{N\,m^{-2}}$ for HETs [1, 26]. Meanwhile, the iEPS developed at MIT has been shown to have a thrust density on the order of 0.1 $\mathrm{N\,m^{-2}}$ [34]. Accion systems has reported thrust densities as high as 2 $\mathrm{N\,m^{-2}}$ with their ionic liquid electrospray propulsion systems [2], competitive with GIEs but still behind HETs. It is important to note that areal thrust density is not the only figure of merit relevant in comparisons between electric propulsion devices. Volume and mass thrust density are also vital in the design of small space systems, and electrosprays in their current form exceed plasma-based EP in these metrics for many of the reasons already discussed, particularly the lack of need for an ionization chamber. Areal thrust density is one of the few metrics in which electrosprays have historically been noncompetitive. To overcome this shortfall, research is being done at MIT and elsewhere to densify ionic liquid electrospray systems.

1.4 Miniaturization and Densification

To increase the thrust density of an electrospray thruster, at least one of two improvements must be made: Increase the magnitude of current capable of being extracted from each individual emitter tip, or increase the number of individual emitters capable of being packed into a given area. The emitted current per tip at a fixed firing potential is driven by the number of emission sites on a tip (typically assumed to be one, but it has been shown that more than one emission site often exists on a single emitter tip [22]) and the physical and geometrical properties of the propellant, tip, and flow path that determine the magnitude of current extracted from each site. Clever design of the emission region and selection of propellant can help maximize the current per tip. For instance, field-emission electric propulsion (FEEP) thrusters utilize liquid metal propellants, the characteristics of which such as high conductivity and low viscosity are favorable for ion emission. FEEPs can emit currents that are often orders of magnitude larger than that of ionic liquid ion sources (ILIS) [25]. However, the larger current comes with the price of needing to supply heat to the stored propellant to keep it in its liquid state, which penalizes overall efficiency and scalability. Instead, electrosprays utilizing ionic liquids can still tailor the properties of emitters and propellants to maximize the current that is physically capable of being emitted.

The other way to increase thruster density is to increase emitter density, i.e. decrease the spacing, or pitch p, between individual emitters to pack larger numbers into equal areas. The theoretical limit to the tip packing density is based on the size of the meniscus from which ions are emitted, which is on the order of 10 nm, as derived in section 1.3. The practical limit is driven by microfabrication capabilities, which are and have been increasing over time. Microfabrication capability has historically followed Moore's Law, which originally stated that the number of components that can be fit into an integrated circuit doubles every year [52]. This trend held true during most of the 1960s [21], and in 1975 Moore revised his prediction to indicate that the rate would slow to doubling the number of components every two years [53],

a trend that has remained approximately true since about 1980 [62]. Moore's Law, although slowing as challenges related to quantum effects become more difficult, has brought the semiconductor industry to the level at which features as small as 10 nm can be fabricated [59].

The state-of-the-art iEPS thrusters developed in the SPL at MIT are fabricated with an emitter pitch of 450 µm, producing arrays much sparser than the theoretical limit. With each tip emitting approximately 200 nA, the resulting thrust density is approximately 0.4 $\mathrm{N\,m^{-2}}$. On the other hand, decreasing emitter pitch to 1 µm can potentially increase thrust density to at least 10^4 $\mathrm{N\,m^{-2}}$, neglecting space charge or viscous flow limitations that may exist.

While the 450 µm emitter technology is a vital step in the long-term development of ionic liquid electrospray propulsion, it is clear that the limit of the technology has not been reached, and advanced fabrication techniques must be leveraged to miniaturize and densify arrays of electrospray emitter tips.

1.4.1 Silicon-Based MEMS Emitters

Silicon-based electrospray thrusters have been designed and tested in the past, but previous instances of silicon electrosprays utilized either capillary [36, 55, 56] or externally-wetted [19, 20, 44, 45] architectures. Externally wetted emitters are not able to be replenished from an external propellant reservoir, making them undesirable for space propulsion applications. Capillary-based electrosprays have been thoroughly studied, tested, and even flown on orbit, but it is difficult to obtain the hydraulic impedance required to achieve purely ionic emission. People have experimented with creating porous silicon substrates starting in the 1980s [24, 67, 66, 17]. Porous substrates permit passive replenishment as well as high impedance, but the porous silicon materials that have been created have extremely small pore sizes (on the order of 1 nm), making the hydraulic impedance too large for any practical electrospray application.

We seek an architecture that would allow for medium-high hydraulic impedance to an external reservoir and that is fabricated in silicon to be able to leverage state-of-the-

art MEMS manufacturing techniques. The specific set of requirements necessitates a new architecture: a combined tip-capillary architecture that transports propellant from a reservoir via microcapillaries etched through a silicon substrate, and an array of textured tips on the surface of the substrate to provide the hydraulic impedance necessary for pure ion emission.

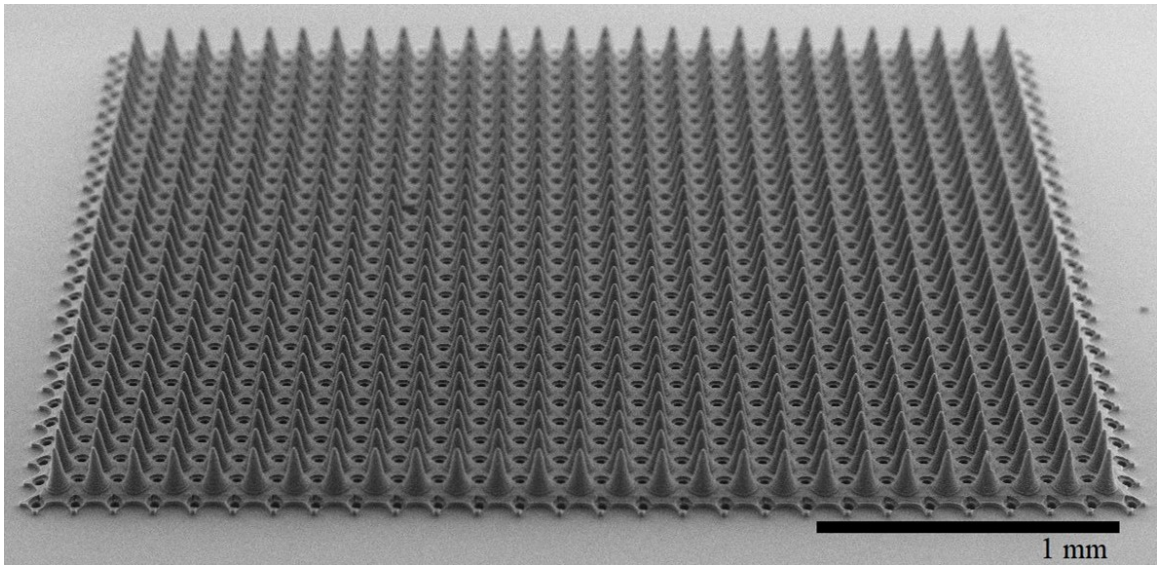

Figure 1-3: SEM image of a 729-tip emitter array with 127 µm pitch.

1.5 Thermal Augmentation

Rather than (or in addition to) increasing the density of emitter arrays, we can address the magnitude of current capable of being extracted from individual emitters. If the current per tip can be increased significantly, thrust density can be increased to compete with or exceed HETs without changing fabrication techniques. The physical principles that control ion emission are complex, but several people and groups have attempted to describe the phenomenon using a set of experimentally validated scaling laws, namely Higuera [25] and Coffman [11]. It is generally accepted that current density from an electrospraying meniscus depends on several properties of the liquid propellant, among other environmental factors and universal constants. Viscosity is one such property that, due it its impact on hydraulic impedance and flow rate, is

believed to share an inverse relationship with emitted current [8]. Here, a methodology is proposed to take advantage of this relationship to thermally augment the current emitted by an electrospray thruster.

By electrically heating the propellant, its viscosity is decreased, resulting in an increase in the emitted current of the thruster at the same firing potential. This has the additional advantage that such an approach would enable the use of porous materials with significantly smaller pore sizes compared to what is used today. Small pore sizes allow for a smoother tip surface, which makes fabrication much more repeatable and operation more reliable. In addition to the increase in performance that this methodology would allow, it will also increase the lifetime of thrusters in a very significant way to enable a variety of commercial and exploration missions. Very small pores are not contemplated right now, since the current (and therefore thrust) that can be extracted when using them is too small to be practical. By implementing a thruster-heating strategy, it should also be possible to eliminate issues related to complexity of the power electronics that otherwise requires significant variations of the high voltage (V) applied to the thruster, which also produces negative effects related to the lifetime of devices, as they can become easily over-stressed. In fact, a simple variable-power heater consuming relatively low power could be implemented, such that the power electronics could operate, for instance, at fixed voltage while throttle-ability is enabled by temperature control alone. Finally, thermal control strategies could be used simply to maintain a constant temperature at which the propulsion system operates most predictably, combating the often large thermal fluctuations that can exist for Earth-orbiting systems.

Increasing thrust density by emitter densification or current augmentation comes with several implications, many of which are not well studied for electrospray thrusters. For instance, it has been predicted that unlike with liquid metal ion sources (LMIS), space charge has a negligible impact on the electric potential surrounding the meniscus in ILIS [25, 6], and therefore space charge effects are typically omitted from ILIS meniscus models. This is typically attributed to the relatively low local current densities that arise from ILIS menisci. However, it is yet to be seen whether techniques

such as thermal augmentation could increase current densities to levels at which a shielding effect occurs that ultimately limits current, as is observed in GIEs and FEEP thrusters.

Additional considerations include effects of temperature on hydraulics, given that electrosprays are extremely sensitive to changes in fluidic impedance and flow rate. Viscosity of ionic liquids is a strong function of temperature, which enables thermal augmentation to begin with. Density has a much weaker dependence on temperature, and surface tension remains nearly constant. That being said, changes in fluid properties over the relevant temperature range could not only impact emission properties but also inform the design of the fluidic network responsible for propellant transport, including the reservoir that stores the propellant. Electroviscous effects are also typically not considered in the design of electrosprays or selection of propellants, but dependencies on temperature of such properties are not well studied for ionic liquids and could have a meaningful impact on the end result.

Finally, thermal augmentation requires investment of power into heating electronics in hopes of a satisfactory return in the form of increased current and therefore thrust. However, several factors influence whether such an investment is worthwhile, including but not limited to the exact properties of the ionic liquid, the efficiency of the electronics and components used for heating, and the thermal properties of thruster components. For example, a thruster that quickly dissipates heat to its surroundings would not be a good candidate for thermal augmentation because the power required to hold the thruster at some elevated temperature may become prohibitive. On the other hand, a well-designed heater system coupled with a well-insulated thruster may potentially see an increase in overall efficiency with a small investment in heating power. Detailed discussion on these factors is included in chapter 3.

Chapter 2

Ultra Dense Silicon Electrospray Thrusters

One method to increase the thrust density of electrospray thrusters is to design thrusters with more densely-packed emitter tip arrays. Assuming each tip emits approximately equal current, the total current, and therefore thrust, produced by the thruster scales directly with the number of tips. By decreasing the emitter pitch and thus fitting more tips in an equal area, thrust density increases. Here, an ultra-dense silicon-based electrospray thruster is discussed and tested to illustrate the usefulness of silicon MEMS technology in the densification of electrospray thrusters.

2.1 Design and Fabrication

The state of the art in electrospray propulsion uses porous glass emitters patterned using laser ablation. While these same fabrication techniques can in principle be used to create thrusters with more densely packed emitter arrays, natural limitations exist to the precision and resolution of laser ablation, so emitter densities approaching the theoretical limit for electrospray propulsion are likely unfeasible. However, extraordinary advances in semiconductor photolithography fabrication techniques have enabled fabrication of incredibly complex planar structures with feature sizes approaching single nanometers. In three dimensions, techniques such as grayscale lithography, which

spatially modulates the exposure of a photoresist mask, can create complex three-dimensional microstructures with smooth facets and resolution better than a single micron [65].

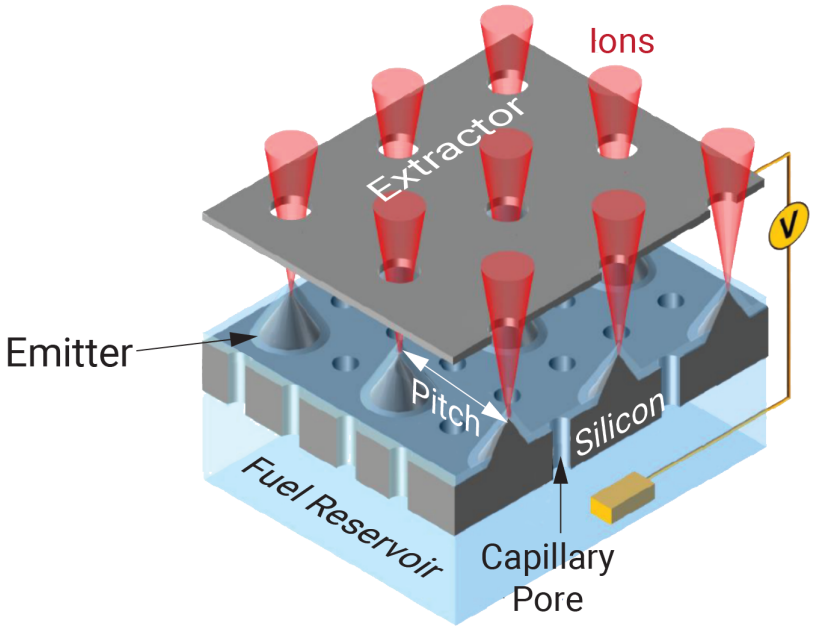

Figure 2-1: The tip-capillary architecture of the ultra-dense silicon-based thrusters, diagrammed to highlight the various components and interfaces.

Details regarding the design and development of the ultra-dense silicon emitters tested here are included in [64]. The combined tip-capillary architecture illustrated in figure 2-1 allows transport of propellant from an external reservoir to an emission site via a fluid circuit comprised of a thin capillary tube and a porous surface layer. A critical design aspect of electrospray emitters utilizing passive propellant transport is their hydraulic impedance, which is the sole determiner of propellant volumetric flow rate. Investigation into the properties of the emitters that determine hydraulic impedance is discussed in the following section.

2.1.1 Emitter Impedance

Hydraulic impedance is a key parameter for electrospray propulsion. As discussed in section 1.3, the magnitude of the propellant flow rate, driven by the hydraulic impedance, determines the emission regime in which the thruster operates. Specif-

ically, pure ionic emission exists only for a relatively limited ranges of impedances. There must be a minimum impedance above which droplet current approaches zero and nearly 100% of the emitted current is due to ions, but excess impedance prevents sufficient replenishment of propellant to the emission site, causing emission to cease altogether.

Hydraulic impedance, Z, of a fluidic circuit is defined as the ratio of pressure drop to volumetric flow rate,

$$Z = \frac{\Delta P}{Q} \tag{2.1}$$

As it travels from the backside of the emitter chip to the apex of the tips, the fluid encounters two primary impedances: (1) due to movement across the front surface and up the tips, and (2) through the capillaries. We first examine the former. At the relevant length scales, it is assumed that capillary forces dominate over gravitational forces, so pressure drops are due to capillarity alone. We also assume that the fluid travels through a thin porous layer on the surface with permeability κ_{ps}. As such, we use Darcy's Law in two dimensions to model the flow.

$$\vec{q_s} = -\frac{\kappa_{ps}}{\mu}\vec{\nabla}P \tag{2.2}$$

where $\vec{q_s}$ is volumetric flow rate per surface area and μ is fluid viscosity. For a rounded conical tip with half-angle θ, height h, and cap radius R_c, the total impedance neglecting gravitational forces can be expressed as [64],

$$Z_{tip} = \frac{\mu}{2\pi\kappa_{ps}\sin\theta}\ln\frac{h\tan\theta}{R_c\cos\theta} \tag{2.3}$$

For flow through the capillaries, envision a straight cylindrical capillary with length L and cross-sectional area A, the inside of which can be modeled as a porous media with permeability κ_{pc}. In this way, we can apply the one-dimensional form of Darcy's Law,

$$Q = \frac{\kappa_{pc} A}{\mu L} \Delta P \tag{2.4}$$

Finding accurate and scalable models for permeability has motivated numerous studies in multiple scientific fields over the past several centuries. If we consider the pores in the a medium to be straight cylindrical tubes running through the bulk material in the direction of fluid flow, the permeability can be expressed as [33],

$$\kappa_{pc} = \frac{\phi^3}{c\tau^2 S^2} \tag{2.5}$$

In equation 2.5, ϕ is porosity or open volume fraction, S is specific surface area or surface area per volume, τ is tortuosity which accounts for complexity of the paths, and c is a constant. Tortuosity is frequently defined as the ratio of the average length of microscopic paths to the length of the macroscopic system in the direction of flow. For simple straight tubes at an angle θ relative to the macroscopic flow, tortuosity is simply $\tau = 1/\cos\theta$. The constant c has complex dependencies, but for straight cylindrical pores $c = 2$. Equation 2.5 is a simple form of the Kozeny model for capillary flow, and it or any representative model for permeability can be substituted into equation 2.6, which gives the expression for impedance of a capillary based on Darcy's Law,

$$Z_{cap} = \frac{\mu L}{\kappa_{pc} A} \tag{2.6}$$

One benefit of using equation 2.5 as our model for permeability is that for vacant capillaries, it is simple to see that $\phi = 1$, $c = 2$, $\tau = 1$, and $S = 2/r$, so $\kappa_{pc} \to r^2/8$ and the impedance is therefore,

$$Z_{poiseuille} = \frac{8\mu L}{A r^2} \tag{2.7}$$

which is exactly the Hagen–Poiseuille equation, which is expected since flow through the capillaries fulfills all assumptions of Hagen–Poiseuille flow.

Neglecting the pressure drop between the top of the capillaries and the base of

the tips, which is assumed to be small compared to the other components, the total hydraulic impedance experiences by the fluid as it travels to the tip apex is therefore,

$$Z_{tot} = Z_{cap} + Z_{tip} = \frac{\mu L}{\kappa_{pc} A} + \frac{\mu}{2\pi\kappa_{ps} \sin\theta} \ln \frac{h \tan\theta}{R_c \cos\theta} \tag{2.8}$$

The result of fabrication is emitter arrays with smooth surfaces and vacant cylindrical capillaries. To satisfy the assumptions in equation 2.8, several treatments are applied to the emitters to (1) create a thin porous layer on the tip surface of permeability κ_{ps}, and (2) create a porous medium inside the capillaries of permeability κ_{pc}. The former is accomplished through roughening of the the silicon surface, and the latter is achieved through sintering glass microspheres inside the capillaries.

Surface Texture

To be able to apply equation 2.3 to the movement of fluid on the emitter surface, we require a porous layer through which the fluid can spread. Several techniques exist to create microscopic surface texture on silicon, but the texture must be properly designed such that the fluid spreads spontaneously. Consider a texture comprised of uniform square posts of width a, height h, and post-to-post spacing b, as in figure 2-2. Define a roughness parameter r to be the ratio of total surface area to projected area, and a planar solid surface fraction ϕ_s to be the ratio of the area of the horizontal post tops to the projected horizontal area. The unit cell that repeats itself is outlined by a dashed box in figure 2-2. We use this unit cell to calculate r and ϕ_s.

$$r = \frac{(a+b)^2 + 4ah}{(a+b)^2} \tag{2.9}$$

$$\phi_s = \frac{a^2}{(a+b)^2} \tag{2.10}$$

Next, we consider a fluid that is dropped onto the surface and fills the space in between the posts. As the fluid spreads, the energy of the system changes as solid-gas interfaces are replaced by solid-liquid interfaces, as in figure 2-3. We can determine

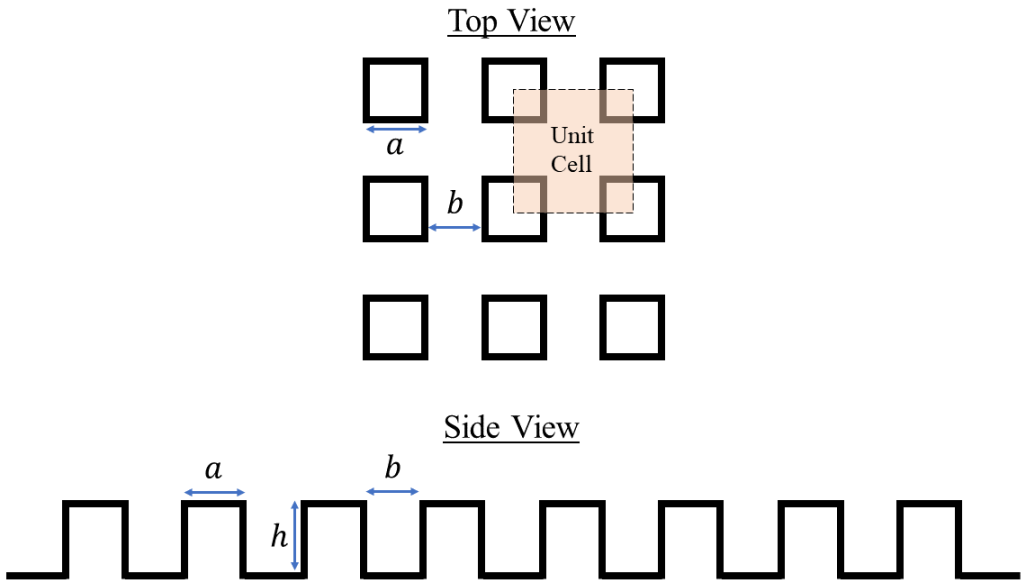

Figure 2-2: Diagram of a simple repeating rectangular post surface texture

if spreading will occur spontaneously by evaluating if the change is energetically favorable. The differential change in energy dE due to the fluid spreading a small distance dx can be written as,

$$dE = (\gamma_{SL} - \gamma_{SG})(r - \phi_s)dx + \gamma(1 - \phi_s)dx \tag{2.11}$$

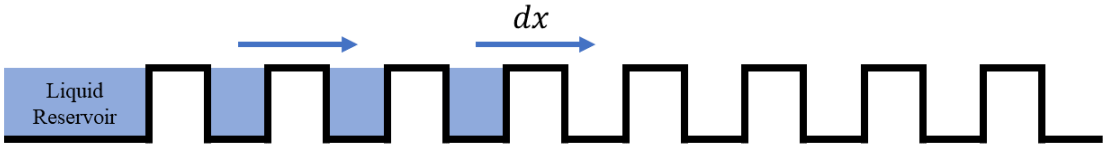

Figure 2-3: Diagram of fluid permeating through a textured surface.

In equation 2.11, γ_{SL}, γ_{SG}, and γ are the surface tensions of the solid-liquid, solid-gas, and liquid-gas interfaces, respectively. The first term represents the energy change due to the conversion of solid-gas interfaces to solid-liquid interfaces, and the second term represents the energy attributed to the addition of a new liquid-gas interface. The change in energy per change in x is therefore,

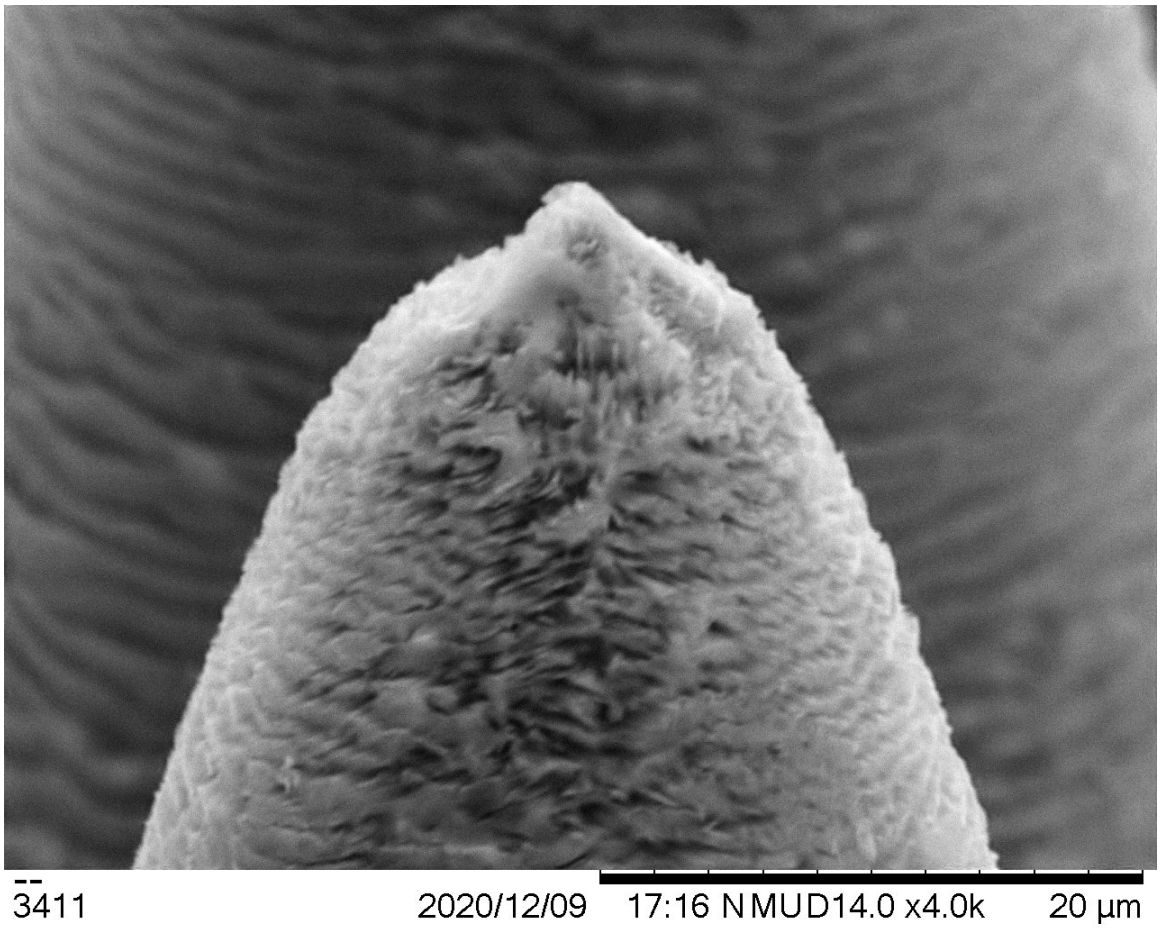

Figure 2-4: Apex of a silicon emitter tip textured using the MACE process.

$$\frac{dE}{dx} = (\gamma_{SL} - \gamma_{SG})(r - \phi_s) + \gamma(1 - \phi_s) = \gamma[1 - \phi_s - (r - \phi_s)\cos\theta_E] \tag{2.12}$$

where θ_E is the equilibrium contact angle for the liquid on a smooth surface, given by Young's equation,

$$\cos\theta_E = \frac{\gamma_{SG} - \gamma_{SL}}{\gamma} \tag{2.13}$$

For spreading to be spontaneous, it is necessary that $dE/dx < 0$, which gives a condition for spontaneous spreading through a textures surface,

$$\cos\theta_E > \frac{1-\phi_s}{r-\phi_s} \tag{2.14}$$

We see that the surface texture must be designed, whether by trial-and-error or otherwise, such that the condition in equation 2.14 is met. Note that θ_E is taken to be a property of the chosen material and fluid, so it is essentially a constant, and therefore ϕ_s and r must be tuned to compete with θ_E.

To add texture to the silicon emitters, black silicon (also known as silicon nanograss) is created. Black silicon refers to a structure of thin spikes etched into a silicon surface. It appears visibly dark due to its tendency to absorb light, thus giving it its name. There are several methods for creating black silicon, but here a metal assisted chemical etching (MACE) process is utilized. Details of the process and formulation of etch conditions are discussed in [64]. A SEM image of a textured emitter tip can be seen in figure 2-4.

Capillary Porosity

The capillaries are sized such that their vacant impedance is small compared to the impedance of moving across the surface. With vacant cylindrical capillaries of length L and radius r, the flow is well-described by the Hagen–Poiseuille equation and the hydraulic impedance can be calculated using equation 2.7. However, if it is desired to add impedance for the purpose of sufficiently restricting the flow in order to achieve stable emission in the pure ion regime, the capillaries can be modified by filling the hollow space with a porous medium. Several methods and materials exist for creating porous media. Even in the relatively narrow field of electrospray propulsion, there is a long history of work in the creation of porous emitter materials. Legge and Lozano fabricated ILIS arrays made from porous tungsten [32, 37], Courtney extensively characterized porous nickel arrays [13, 14, 16], and Coffman spearheaded the transition to porous glass emitters [12, 10]. Sintering glass microspheres is now a common and simple methods for creating porous media with several advantages over metals [23], including but not limited to the dielectric nature of glass, its relatively

low melting point, and compatibility with efficient and precise etching techniques like laser ablation. Creating porous glass columns inside of silicon capillaries for electrospray manufacturing, similar to what is being attempted here, was studied by Xie in 2013 [71].

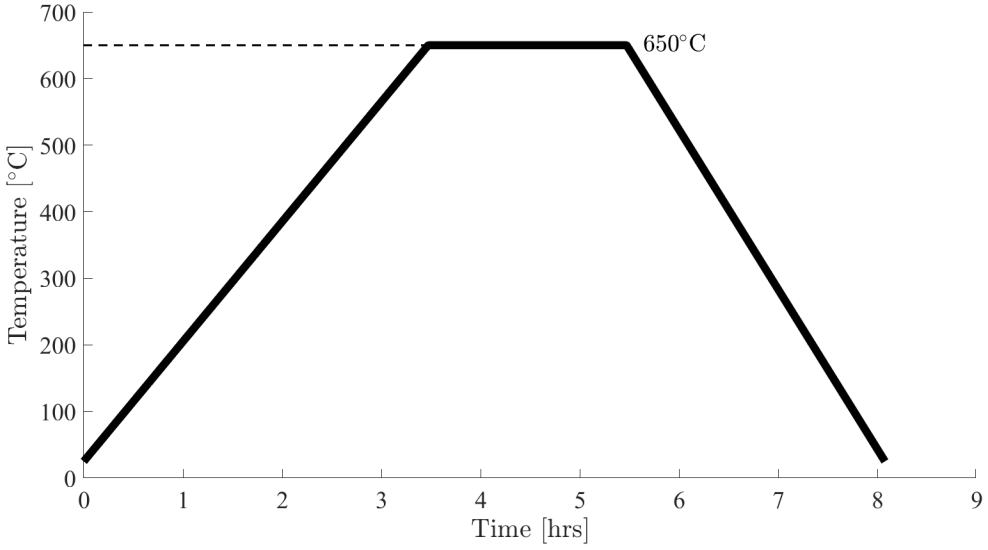

Figure 2-5: Temperature profile used to sinter soda-lime glass beads inside the emitter capillaries to form a porous structure.

To create a porous column inside the capillaries of the silicon emitters, soda-lime glass microspheres with a median diameter of 4 µm are used. Soda-lime glass has benefits over other types of glass like silica in that it is extremely inexpensive and softens at relatively low temperature (600-700°C compared to $>$ 1500°C for silica). The capillaries are filled with microspheres from the backside of the emitter. A small amount of dry glass powder is placed onto the emitter backside, and it is forced into the capillaries by either a soft instrument or a gloved finger. The process is repeated several times per emitter to ensure the capillaries are filled with microspheres. The emitters are then sintered by heating in a furnace at 600-700°C for 2 hours. At these temperatures for this duration, the glass spheres begin to soften and coalesce. The sintering profile, shown in figure 2-5 with a heating ramp at 3°/min, cooling ramp at 4°/min, and dwell time of 2 hours is based on previous work done by Xie [71] and later Bost [3], who sought to create similar porous media with soda-lime glass.

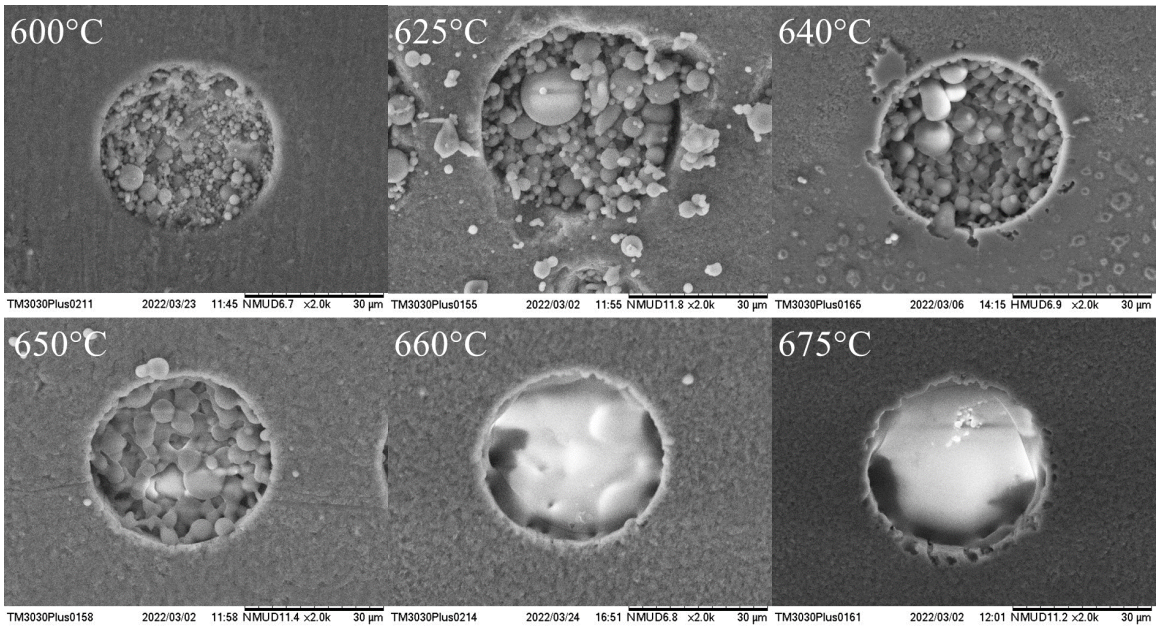

Figure 2-6: Results of sintering glass microspheres at different dwell temperatures between 600°C and 675°C.

Emitters sintered at different dwell temperatures between 600°C and 675°C were fabricated to find the optimal recipe. Figure 2-6 shows the resulting porous structures. It can be seen that at the lower dwell temperatures, the microspheres do not soften and coalesce, while at the higher temperatures they form a solid plug in the capillary. The ideal porous structure forms when the spheres are allowed to soften and neck together without melting completely, which can be seen to occur at dwell temperatures between 640°C and 660°C, with 650°C being a satisfactory balance.

The combined effects of the surface texture and capillary impedance create the circumstances for ideal emitter wetting in which the propellant is contained in the porous surface layer and travels from the emitter backside to the tip apex at rates compatible with pure ionic emission. A SEM image of an ideally-wetted emitter array is shown in figure 2-7. Here, the propellant conformally coats the surface without excess fluid accumulation that can lead to shorting between the emitter and extractor. Section 2.2.3 discusses examples of cases in which ideal wetting is not achieved and the detrimental effects that non-ideal wetting can have on thruster lifetime.

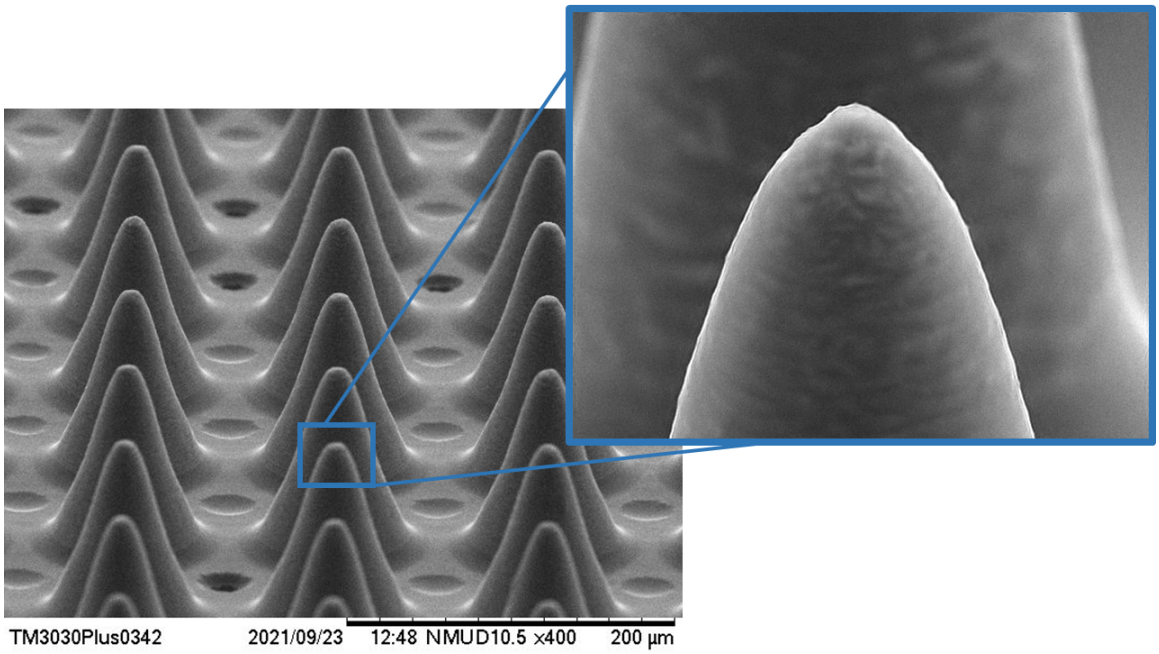

Figure 2-7: SEM image of an ideally-wetted emitter array.

2.2 Characterization of Integrated Silicon Thrusters

The work of Siegel [64] culminated in test firing of the silicon emitters onto a solid plate extractor. Since the solid extractor was without apertures, it could be shown that the emitters were capable of emitting current, but no thrust was produced as the ions impinged directly onto the plate instead of leaving the system as exhaust.

To produce thrust, a semi-transparent extractor must be used to apply the potential difference in such a manner that emitted ions can accelerate through the extractor apertures and be expelled from the thruster. An extractor grid was designed to be fabricated from silicon so that they can be efficiently mass-produced using the same silicon MEMS fabrication technology used to fabricate the emitters. The integrated thrusters are assembled by aligning the extractor apertures to the emitter tips using a multi-axis micro manipulator system, and precise spacing between the emitter and extractor is maintained using glass spacers.

2.2.1 Facilities Overview

The thrusters are tested primarily in the Turbovac vacuum chamber in the SPL. Turbovac is equipped with a mechanical roughing pump and two turbomolecular pumps. Thrusters are tested at pressures below 5×10^{-6} Torr. The chamber is outfitted with various diagnostic instruments, and during testing thrusters are mounted on a rotational stage such that the beam can be aimed at different instruments without breaking vacuum.

High voltage is supplied to the thruster using a Matsusada AP-3B1 high voltage amplifier, and currents through the power supply and through the extractor electrode are measured independently using Analog Devices AD210AN isolation amplifiers. All signals, including voltages, currents, and miscellaneous measurements are collected using a National Intruments USB-6229 DAQ and logged using custom software.

In addition to being able to collect current-voltage (IV) data, the Turbovac chamber is outfitted with a retarding potential analyzer (RPA), a time of flight mass spectrometer (TOF), and a Faraday cup. Each instrument is positioned at a different angle relative to the chamber centerline so that the thruster can be rotated to face any one of them at a time. The details of each of these instruments and the information about thruster performance that they reveal are listed in the following sections.

Current-Voltage Characteristic

The current-voltage response of the thruster is characterized by measurement of the ion beam current emitted by the thruster in response to an applied voltage. The results of such experiments indicate the startup voltage of the thruster and is used, in conjunction with other measurements, to evaluate the thrust-to-power ratio achievable by the thruster at different operating points. In addition, a thruster IV curve reveals its ability to be throttled by modulation of the voltage to control the emitted current, which is crucial information for the design of the power electronics that will be used to operate the thrusters.

Retarding Potential Analysis

Retarding potential analysis utilizes semi-transparent grids, which can be biased to variable potentials, to determine the energy of the charged particles that exist in the beam. Behind the biased grids sits a Faraday cup for current collection, so the magnitude of current collected behind the grids varies with the potential of the grids. Ions with insufficient energy to overcome the potential field are retarded, while ions with sufficient energy are collected. By performing sweeps on the grid potential, an energy spectrum of the beam particles is obtained, yielding estimates for the efficiency of the ion acceleration process.

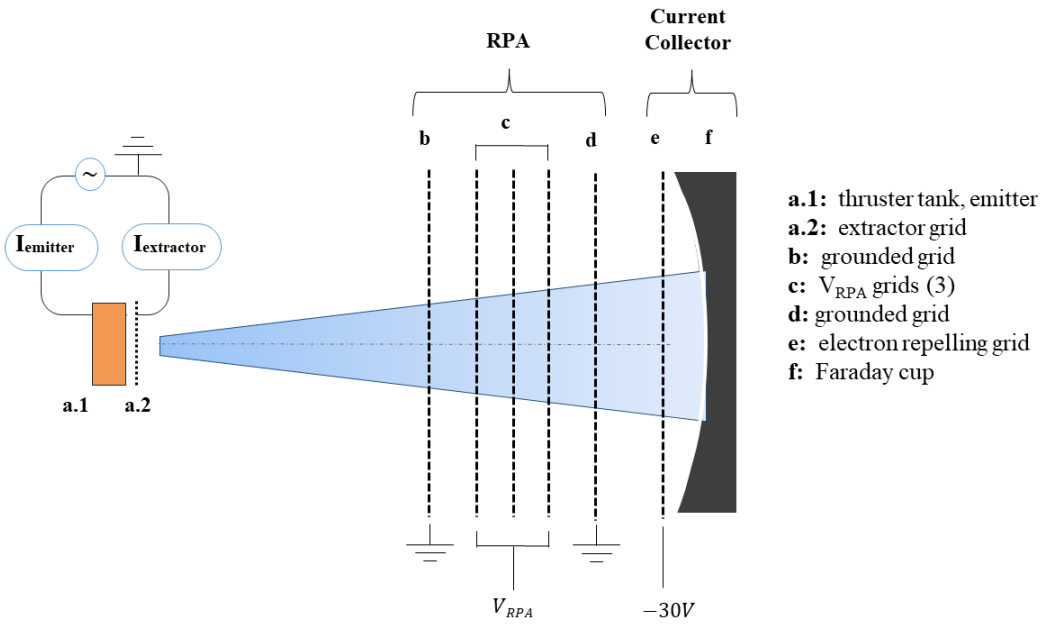

Figure 2-8: Diagram of the RPA used in the electrospray tests in the SPL

Figure 2-8 shows a diagram of the RPA used in these tests. Several grids are placed in series, including the high-voltage retarding grid, grounded grids, and an electron repelling grid biased to −30 V to keep secondary electrons produced by collisions with the upstream grids from interfering with the current signal. RPA measurements also give insight into ion fragmentation processes that occur inside and outside the thruster. Fragmentation occurs when a solvated ion, or an ion attached to a single or cluster of neutral molecules, breaks up into a neutral molecule and a lighter ion.

Table 2.1: Most common ion clusters present in EMI-BF_4 ion beams.

Polarity	**Degree of Solvation**	**Mass [amu]**
Positive (EMI^+ cation)	$n = 0$	111.2
	$n = 1$	309.2
	$n = 2$	507.2
Negative (BF_4^- anion)	$n = 0$	86.8
	$n = 1$	284.8
	$n = 2$	482.8

These fragmentation events show up in RPA curves because when a cluster breaks apart, the sum of the energies of the resulting fragments is equal to the total pre-fragmentation energy of the cluster, which is approximately the energy gained during acceleration through the applied electric field (the beam energy).

If a cluster fragments outside of the thruster when it is no longer accelerating (the field-free region), its post-fragmentation energy will be a predictable fraction of the beam energy, depending on the degree of solvation of both the pre- and post-fragmentation ions. The most common species present in the beam are typically isolated ions (monomers, degree of solvation $n = 0$), ions attached to a single neutral particle (dimers, $n = 1$), and ions attached to a cluster of two neutrals (trimers, $n = 2$). Table 2.1 gives the masses of each cluster type for both positive EMI^+-based ions and negative BF_4^--based ions.

Based on the most plentiful species in the beam, the most common fragmentation events are expected to be fragmentation of trimers into monomers, dimers into monomers, and trimers into dimers. Since clusters that fragment outside of the acceleration region have reached their terminal velocity, the energy fraction of the fragmented ion is equal to its mass fraction relative to the original cluster. These mass fractions for EMI-BF_4 are given in table 2.2. For field-free region fragmentation events, the mass fractions are equal to the energy fractions.

Clusters that fragment inside the acceleration region have a more complex energy distribution. For a singly-charged parent cluster that breaks into a neutral particle and a singly-charged child cluster, the charged species experiences different acceler-

Table 2.2: Common fragmentation events in EMI-BF_4 ion beams.

Polarity	Fragmentation Event	Mass Fraction
Positive (EMI^+ cation)	$n = 2 \rightarrow n = 0$	0.22
	$n = 1 \rightarrow n = 0$	0.36
	$n = 2 \rightarrow n = 1$	0.61
Negative (BF_4^- anion)	$n = 2 \rightarrow n = 0$	0.18
	$n = 1 \rightarrow n = 0$	0.30
	$n = 2 \rightarrow n = 1$	0.59

ation magnitudes before and after the fragmentation event. Therefore, the energy fraction of the fragmented species is not a simple mass fraction. Rather it depends on both the initial and final masses and the location in the acceleration region at which fragmentation occurs. Because fragmentation events are typically distributed spatially throughout the acceleration region, the result is a distribution of ion energies that fall between the energies associated with field-free fragmentation events listed in table 2.2.

Time of Flight Mass Spectrometry

Time of flight mass spectrometry is used to determine the average charge-to-mass ratio of the beam, an indicator of specific impulse. It is achieved by using high-resolution instruments to measure the time for particles in the beam to traverse a known distance. The velocity of a particle accelerated from rest through a potential difference has a one-to-one relationship with its charge-to-mass ratio. Since the beam is heterogeneous, TOF is used to obtain a spectrum of all charge-to-mass ratios that exist in the beam, and average properties like thrust and specific impulse can be deduced therein by integration.

Figure 2-9 shows a diagram of the SPL TOF instrument. The ion beam is directed through an aperture near the ion source where it encounters a deflecting gate biased to $\pm$950 V and controlled by a square waveform to start and stop the beam's path toward the downstream detector in regular intervals. The beam travels through a long isolated tube (length approximately 1 m) before its signal is amplified by a

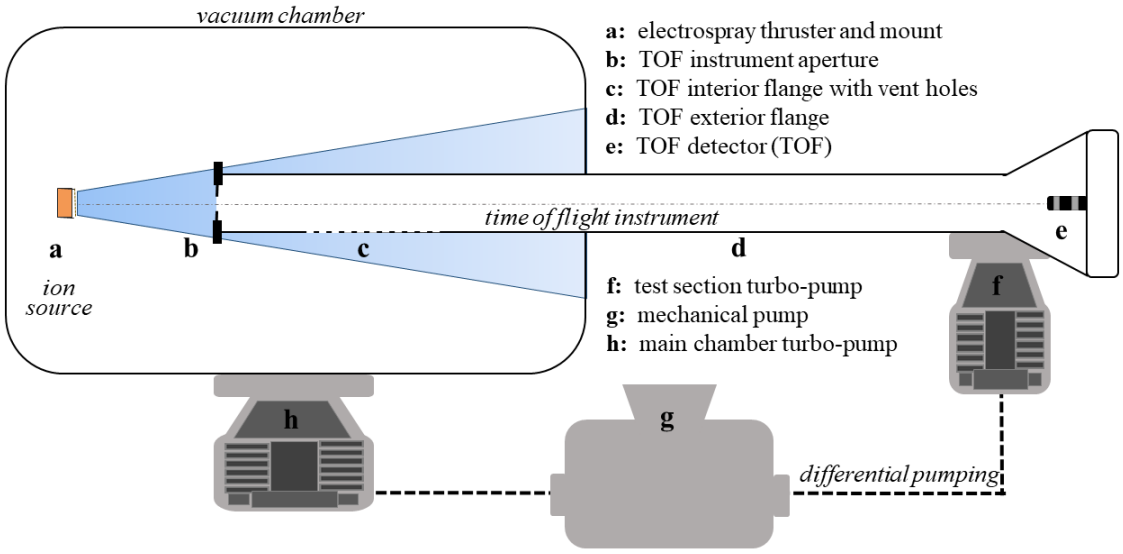

Figure 2-9: Diagram of the TOF used in the electrospray tests in the SPL

Channeltron channel electron multiplier (CEM), which amplifies the signal with a gain of at least 10^7.

TOF measurements are used to calculate properties of the beam by balancing an ion's electric potential energy at emission with its kinetic energy after acceleration.

$$qV_0 = \frac{1}{2}mc^2 \tag{2.15}$$

From equation 2.15, we can find an ion's expected velocity c as a function of its charge-to-mass ratio q/m, or equivalently its q/m as a function of c,

$$\begin{aligned} c &= \sqrt{2\frac{q}{m}V_0} \\ \frac{q}{m} &= \frac{c^2}{2V_0} \end{aligned} \tag{2.16}$$

The mass flow rate of ions out of the thruster can be related to the emission current I and the charge-to-mass ratio of the charged species responsible for the current. For a single species being emitted from the thruster,

$$\dot{m} = \frac{dm}{dt} = \frac{dm}{dq}\frac{dq}{dt} = \frac{1}{q/m}I \tag{2.17}$$

So, we can combine equations 2.16 and 2.17, along with the expression for thrust of a rocket engine in vacuum (equation 1.6), to obtain,

$$F = \dot{m}c = \frac{1}{q/m}I\sqrt{2\frac{q}{m}V_0} = I\sqrt{\frac{2V_0}{q/m}} \tag{2.18}$$

If multiple species exist in the beam, the contribution of each species to thrust is given by equation 2.18. Therefore, the total thrust is a summation of these contributions,

$$F = \sum_i I_i\sqrt{\frac{2V_0}{(q/m)_i}} \tag{2.19}$$

A raw TOF signal gives current as a function of time t rather than q/m directly. The velocity, c, of the ion is related to the known length of travel, L, and the measured time of travel, t, by $c = L/t$. So, we can combine equation 2.19 with equation 2.16 and $c = L/t$ to write,

$$F = \sum_i I_i\frac{2V_0}{L}t_i \tag{2.20}$$

Or for a continuous spectrum of species, the summation can be written as an integral

$$F = \frac{2V_0}{L}\int_0^\infty I(t)dt \tag{2.21}$$

Equation 2.21 can be used to indirectly estimate thrust from a TOF measurement. Note we must assume that all species are singly-charged ions. If a significant amount of multiply-charged ions or neutral species exist in the beam, equation 2.21 becomes decreasingly accurate. We can perform a similar derivation, starting with equation 2.17, to estimate $\dot{m}$ as a function of $I(t)$. Omitting the intermediate steps for brevity, the result is,

$$\dot{m} = \frac{4V_0}{L^2}\int_0^\infty I(t)tdt \tag{2.22}$$

Furthermore, equations 2.21, 2.22, and 1.6 can be used to compute estimates for thrust, mass flow rate, and specific impulse of an electrospray thruster given a TOF signal of the form $I(t)$.

Angular Beam Distribution

Beam divergence information is acquired by measuring the current density of the thruster plume at different angles relative to the thruster centerline. Beam divergence measurements are a key contributor to estimates of overall thruster efficiency, as only the component of ion velocities normal to the thruster face contribute usefully to trust.

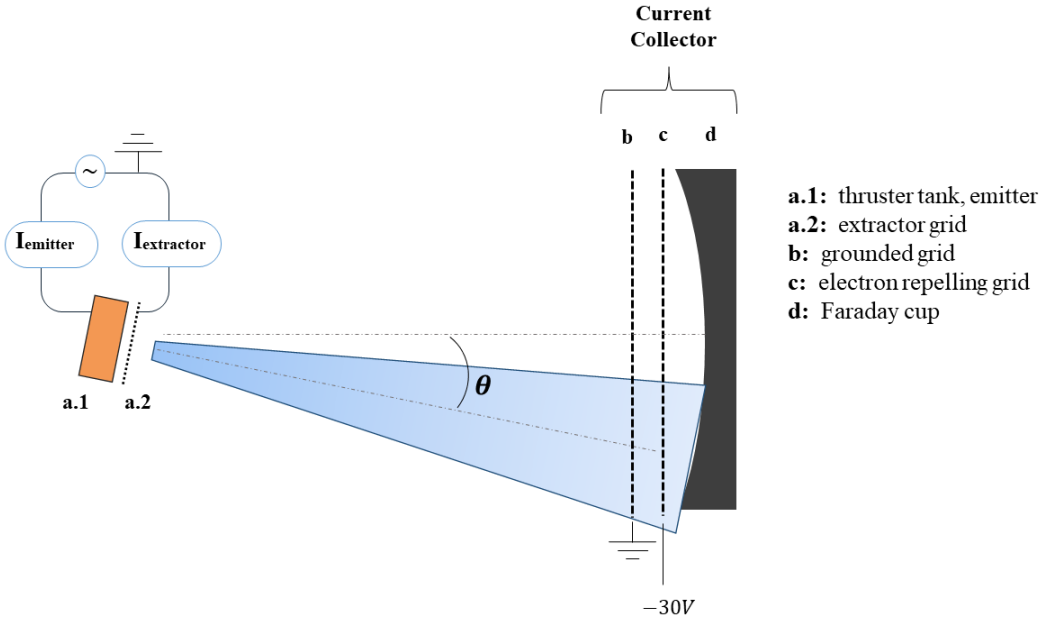

Figure 2-10: Diagram of the angular beam distribution measurement setup used in the electrospray tests in the SPL

Beam divergence data is measured by firing the thruster at a Faraday cup current collector and varying the angle θ between the thruster and collector centerlines. The result is a measure of current as a function of θ.

2.2.2 Test Results and Performance Metrics

Current-voltage curves were measured by applying a triangular voltage waveform to the emitter electrode with an amplitude of 1300 V and a period of 60 seconds. Current outputted by the emitter and intercepted by the extractor are independently measured as voltage is swept, generating a relationship between voltage and current. The waveform is repeated three times and the data are averaged. The resulting IV curve is shown in figure 2-11.

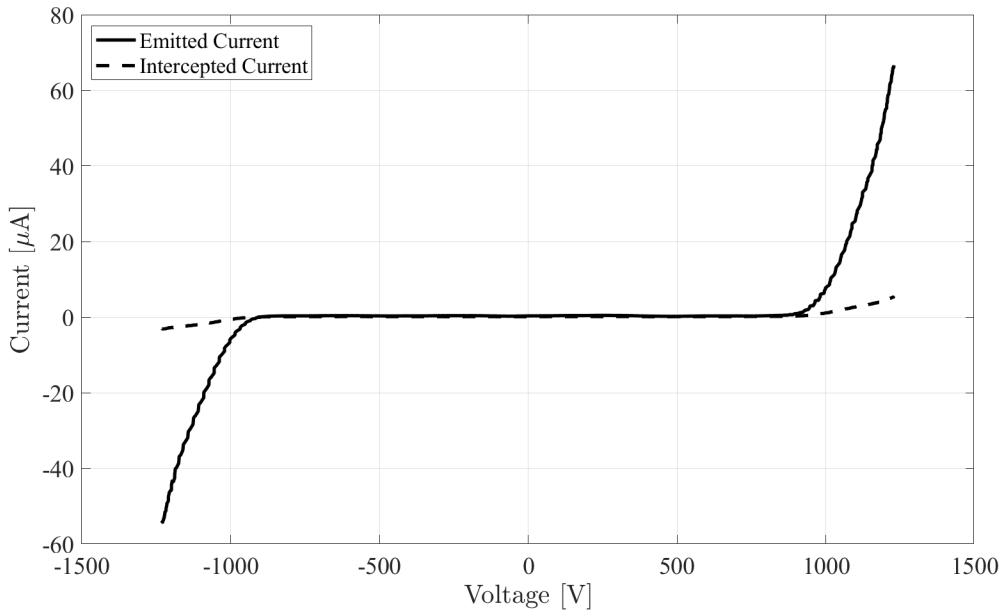

Figure 2-11: Current-Voltage characteristic curve of an ultra-dense silicon thruster.

Key metrics attainable from the IV curve include startup voltage and transmission efficiency, or the efficiency of the process of extracting ions through the extractor grid. The observed startup voltage based on figure 2-11 is approximately 800 V. The expected startup voltage can be estimated based on the known geometry of the system using equation 1.10. With $R_c = 5$ µm, $d = 100$ µm, and $\gamma = 0.05$ N m^{-1} for EMI-BF_4, we expect $V_{start} \approx 750$ V, showing that equation 1.10 is a very useful order of magnitude estimate for V_{start}. Since the properties of EMI-BF_4 are well known and the fabrication techniques utilized result in extreme precision in R_c, the underestimation here can most likely be attributed to imperfections in emitter-extractor spacing, d,

which for these prototype devices is accomplished using insulating spacers with a relatively large thickness tolerance. It is clear that even with the crude assumptions made in the derivation of equation 1.10, it is a reasonable predictor of startup voltage.

Transmission efficiency is defined as

$$\eta_{tr} = \frac{I_{em} - I_{int}}{I_{em}} \tag{2.23}$$

Transmission efficiency can be interpreted as the fraction of emitted current that contributes to thrust, since current intercepted by the extractor does not exert a net force on the thruster. The IV curve in figure 2-11 yielded an average transmission efficiency of $\eta_{tr} = 0.907$.

Retarding potential analysis measurements are taken with the thruster firing in a steady state condition. The RPA measurement for the silicon thruster was taken with the thruster firing at potential $V_0 = 1300$ V and emitting a steady current of approximately 71 µA. With the thruster firing into the RPA diagrammed in figure 2-8, a triangular voltage waveform is applied to the retarding grip. V_{RPA} is swept between -200 V and $+1500$ V to encompass all ion energies expected in the beam. Current collected by the Faraday cup downstream of the retarding grid is collected, yielding a relationship between V_{RPA} and collected current. The resulting RPA curve is shown in figure 2-12.

RPA measurements yield information about fragmentation events occurring both inside and outside of the thruster as well as the efficiency with which the thruster converts electric potential energy to ion kinetic energy. This efficiency is known as energy efficiency, and it is the ratio of the beam potential to the applied firing potential.

$$\eta_E = \frac{V_B}{V_0} \tag{2.24}$$

where V_B and V_0 are the beam potential and applied firing potential, respectively. The beam potential can be estimated as the maximum peak in the ion energy spectrum, which is found by taking a derivative of the RPA curve in figure 2-12 with respect to

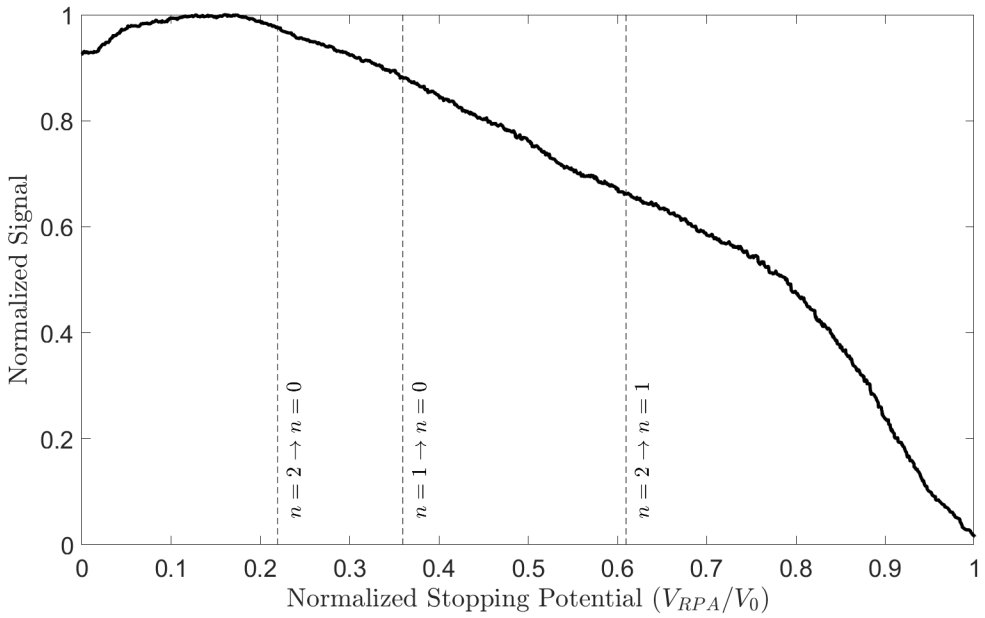

Figure 2-12: RPA curve of an ultra-dense silicon in the positive polarity.

V_{RPA}. Since a derivative of a discrete signal must be performed, the quality of the signal and the amount of noise present can greatly impact the estimate for η_E, and it is therefore difficult to obtain highly accurate η_E measurements. The beam potential was found to be approximately $V_B \approx 1170$ V at an applied potential of $V_0 = 1300$ V, yielding an energy efficiency of approximately $\eta_E \approx 0.900$.

Time of flight measurements, like RPA measurements, are acquired with the thruster firing at a steady condition. The TOF measurement for the silicon thruster was taken with the thruster firing at approximately the same conditions as it was during the RPA measurement. The beam is directed through an aperture toward the TOF instrument, and the gate is enabled to interrupt the beam at regular intervals. Downstream, the CEM current amplifier collects current as a function of time after each gate opening. A TOF curve of one of the silicon thrusters is shown in figure 2-13.

As discussed in section 2.2.1, several key performance metrics can be estimated from TOF results, including thrust, specific impulse, mass flow rate, and polydispersive efficiency. Polydispersive efficiency is a measure of energy losses due to accelerat-

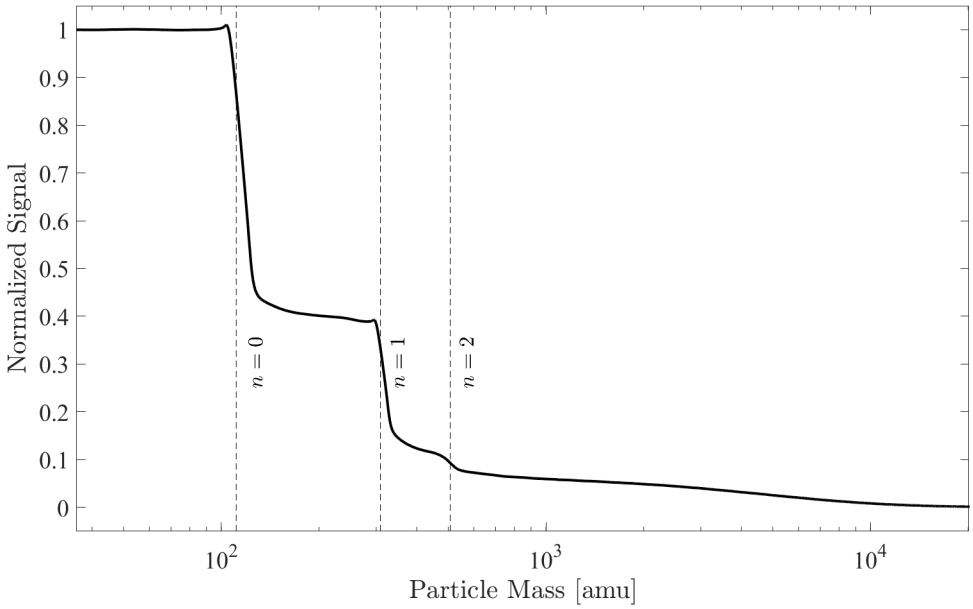

Figure 2-13: TOF curve of an ultra-dense silicon in the positive polarity.

ing ions and clusters of varying specific charge, and it is one of the primary efficiency losses in electrospray thrusters. Polydispersive efficiency can be estimated using TOF data from equation 2.25 [51].

$$\eta_p = \frac{F_{TOF}^2 / 2\dot{m}_{TOF}}{I_{em} V_0} \tag{2.25}$$

Polydispersive efficiency is a significant loss in electrosprays because there is frequently a polydisperse composition of ions in the beam, and the energy spent accelerating the faster ones is greater than the extra thrust derived from them. The TOF curve in figure 2-13 yielded a polydispersive efficiency of $\eta_p = 0.506$. Thrust, specific impulse, mass flow rate estimates from the TOF curve are listed in table 2.3.

Finally, the beam divergence measurements were taken with the thruster firing at steady state with $V_0 = 1000$ V and $I_{em} = 32$ µA. The thruster is fired at the Faraday cup while mounted on a rotational stage, and the angle between the thruster and collector centerlines is linearly swept between $\pm 45°$ a total of six times and the collected current as a function of angle θ is recorded and averaged across the six repetitions. The beam divergence data for the silicon thruster is presented in figure

2-14.

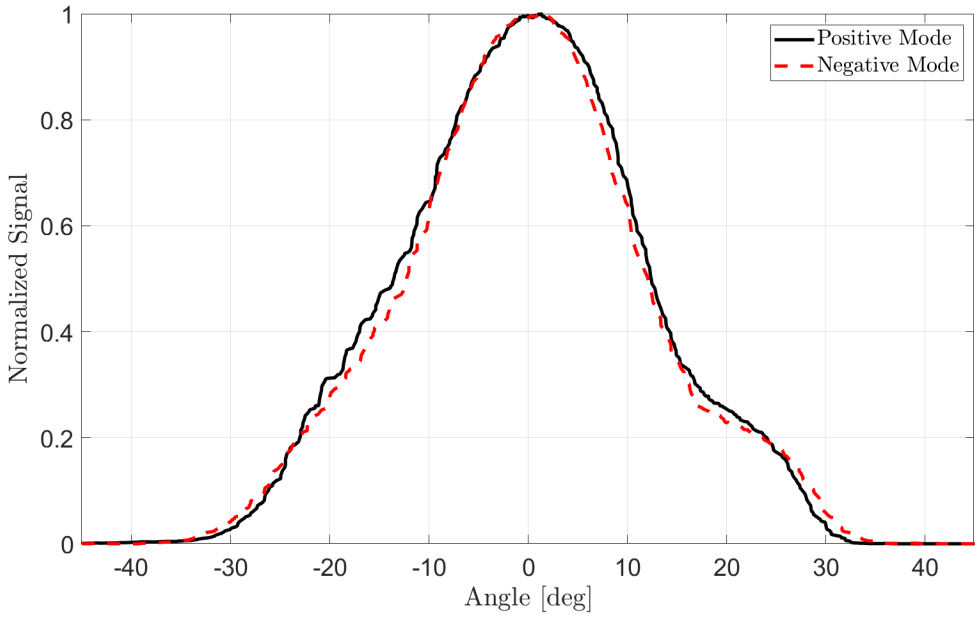

Figure 2-14: Angular beam distribution of an ultra-dense silicon thruster in both the positive and negative polarities.

From the beam divergence measurement, we are able to ascertain the angular efficiency of the thruster, which is a projection of the beam's momentum along the axis normal to the thruster face compared to the ideal case in which the entire beam was emitted normal to the thruster face. To estimate the angular efficiency, the beam is assumed to be axisymmetric with composition and properties that do not vary with time or angle. With these assumptions, the angular efficiency can be calculated as,

$$\eta_\theta = \left(\frac{\int_0^{\frac{\pi}{2}} I(\theta) \cos\theta \sin\theta d\theta}{\int_0^{\frac{\pi}{2}} I(\theta) \sin\theta d\theta} \right)^2 \tag{2.26}$$

Prior to computing η_θ using equation 2.26, the beam divergence data was smoothed and centered around a central firing angle. The central angle θ_c was computed by numerically solving equation 2.27.

$$\int_{-\frac{\pi}{2}}^{\theta_c} I(\theta) d\theta = \int_{\theta_c}^{\frac{\pi}{2}} I(\theta) d\theta \tag{2.27}$$

The angular efficiency for the silicon thruster at this operating point was estimated

Table 2.3: Performance metrics of ultra-dense silicon thrusters from diagnostic data. Data is for positive mode only.

Metric	**Estimate**	**Units**
F	6.3	µN
$\dot{m}$	0.43	$\mu g\, s^{-1}$
I_{sp}	1499	s
η_{tr}	0.907	-
η_E	0.900	-
η_p	0.506	-
η_θ	0.919	-
η_T	0.344	-

to be $\eta_{\theta+} = 0.919$ $\eta_{\theta-} = 0.909$ for the positive and negative modes, respectively.

The total thruster efficiency, η_T, is the percentage of supplied electrical power that is converted to usable beam power, and it can be estimated using equation 2.28, as in [40] and [57].

$$\eta_T = \frac{P_T}{P_E} = \frac{\frac{1}{2}F^2/\dot{m}}{IV_0} = \eta_i \eta_{tr}^2 \eta_\theta \eta_E \eta_p \tag{2.28}$$

The ionization efficiency η_i is typically taken as unity for electrospray thrusters, which amounts to an assumption that no neutral species evaporate from the ionic liquid. Taking the individual efficiencies calculated above, the total thruster efficiency can be estimated to be $\eta_T = 0.344$. The total efficiency for the tested thrusters is low compared to published efficiencies for EMI-BF_4 electrosprays in the pure ion regime, estimates for which range from about 60% [57] to as high as 90% [40]. However, the ultra-dense silicon thruster is in a prototypical state and far from optimized. Future work will iterate on the design to achieve better fabrication precision, tailored fluid control, and improved and more repeatable assembly/alignment processes. These future iterations will be expected to improve in areas that contribute most detrimentally to efficiency, such as transmission and polydispersion. Table 2.3 gives a complete list of the performance metrics and efficiencies for the ultra-dense silicon thruster in the positive mode.

2.2.3 Failure Mechanisms

Several failure modes were identified during the characterization of the ultra-dense silicon electrosprays, many of which are directly related to the known life-limiting mechanisms of electrosprays discussed in section 1.3.2. While the technology is maturing, it is crucial to identify the known failure mechanisms so they can be mitigated now or in the future. The three common failure modes observed during testing and discussed below are thruster shorting, emitter flooding, and electrochemical wear. These failure modes did not prevent the acquisition of the useful performance data discussed in section 2.2.2, but they did make it more difficult to collect long-duration firing data. Long-duration thruster tests will be addressed in future work.

Thruster Shorting

Shorting of the thruster between the emitter and extractor electrodes was the most common failure mechanism. A short occurs when ionic liquid bridges the gap between the emitter and extractor, allowing current to flow through the thruster circuit nearly unimpeded. When a short occurs, a potential difference between the emitter and extractor is no longer able to be sustained, and the thruster is rendered inoperable. In addition, the relatively large current that is allowed to flow through the small ionic liquid bridge results in significant ohmic heating, causing the propellant to decompose and the emitter tips to deform. Evidence of a short circuit inside one thruster is shown in figure 2-15. A short is easily identified by the dark products of thermal decomposition of the propellant, which can often be seen on both the emitter and extractor after this type of failure has occurred.

Multiple root causes can result in thruster shorting, including insufficient spacing between the emitter tips and extractor grid, poor alignment, incorrect surface texture or hydraulic impedance, and emitter flooding, the latter of which will be discussed in more detail below. Preventing thruster shorting altogether is difficult because as the thruster fires over long durations, the likelihood of propellant accumulation increases. However, prevention of premature shorting is possible by ensuring that the emitters

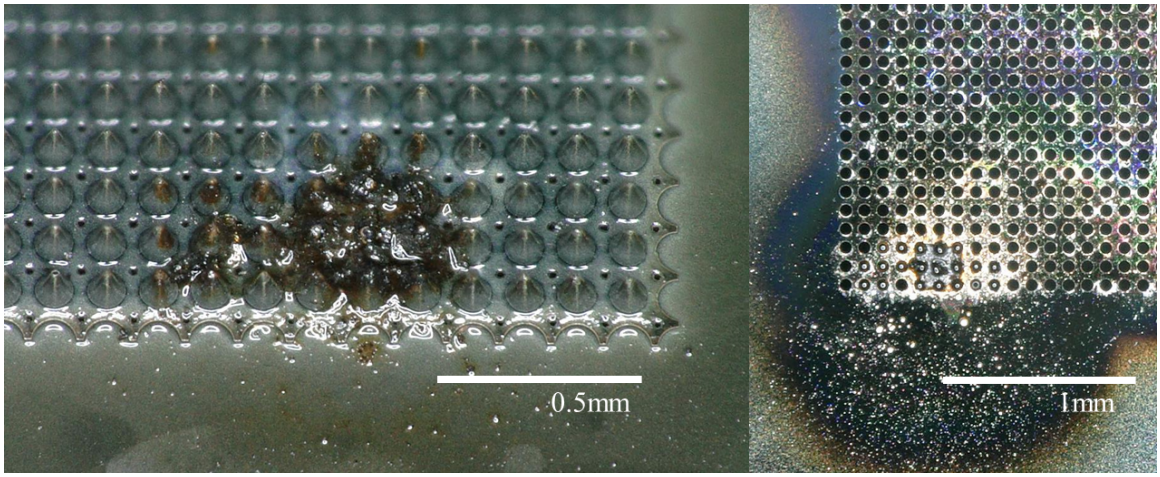

Figure 2-15: Images of a thruster that experienced shorting. Left: Emitter in the area of shorting showing burned down tips and pyrolyzed propellant. Right: Corresponding spot on the extractor grid showing evidence of conact with propellant and high temperatures.

are providing the correct hydraulic impedance and that thruster assembly is done carefully and with high precision.

Emitter Flooding

Flooding of the emitter occurs when excess propellant accumulates on the top surface of the emitter chip, sometimes submerging the tips and preventing ion emission from being possible, and increasing the likelihood of a short circuit. A SEM image of a flooded emitter is shown in figure 2-16. In this extreme example, the tips in the wetted areas are almost entirely submerged, making them unable to emit ions. The failure mode seen in figure 2-16 also shows a fraction of the emitter that is not wetted at all. Observance of excess propellant in one area and a complete lack of propellant in another indicates that a likely root cause of the failure was improper surface conditions that did not favor spreading. However, several other factors can contribute to emitter flooding. For instance, gas such as air that is trapped in pores or capillaries during propellant filling can force excess propellant onto the emitter surface when the thruster is depressurized and the gas tends to escape. For these reasons, ensuring proper surface texture and filling the thrusters in a controlled environment is critical to prevent these types of failure modes.

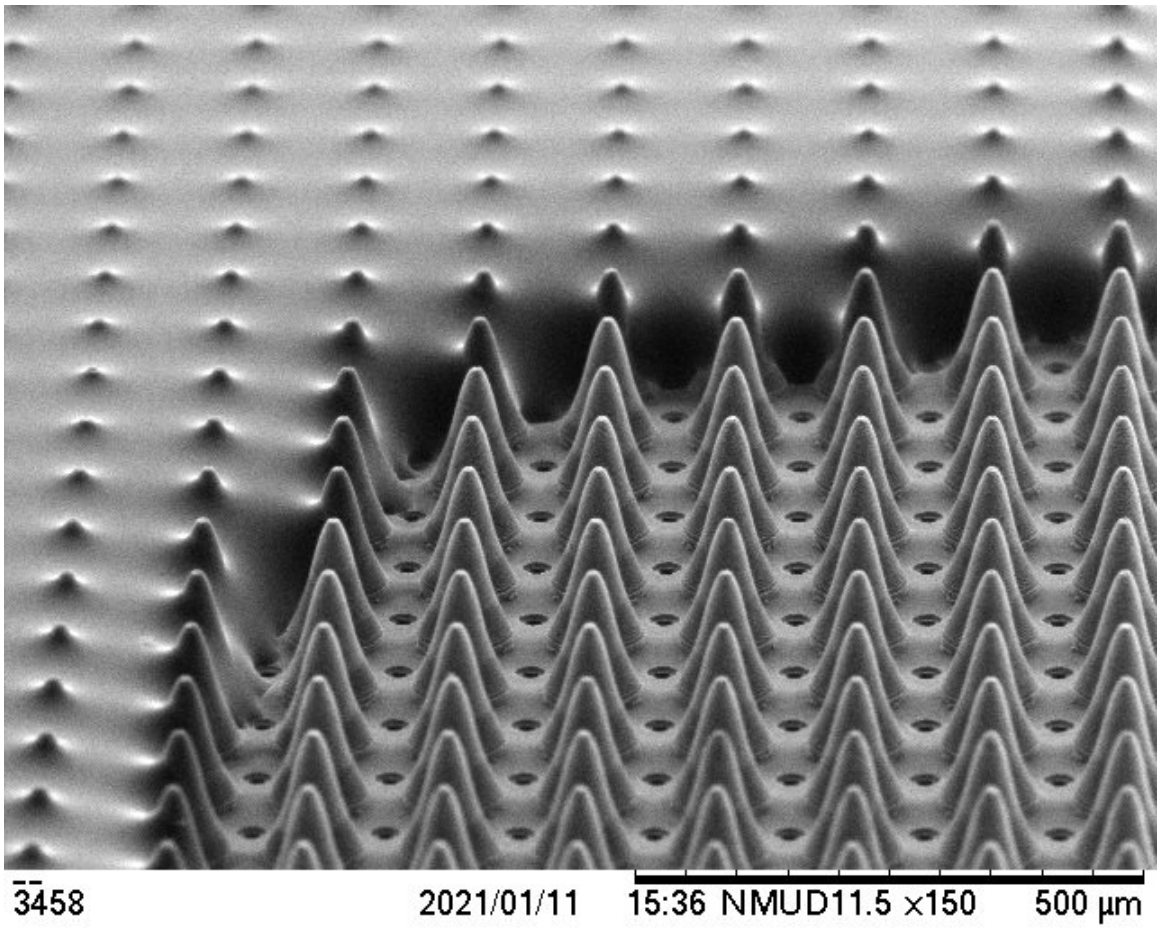

Figure 2-16: SEM image of an emitter that experienced flooding. Only the apex of the tips apexes of the tips are visible in the wetted regions.

Electrochemical Wear

The phenomenon of electrochemical wear is discussed in section 1.3.2. Firing a thruster in a single polarity causes an electrical double layer (EDL) to form at the interface between the electrode surface and the propellant. When the EDL saturates with charge, an electrochemical reaction occurs, transferring electrons across the interface while consuming the propellant into decomposed products. If these Faradaic reactions occur near the apex of the emitter tips, the tip surfaces can become deformed, degrading their performance as ions emitters. Figure 2-17 shows a SEM image of an emitter that appears to have undergone electrochemical wear.

Prevention of electrochemical wear is difficult due to the complex nature of the

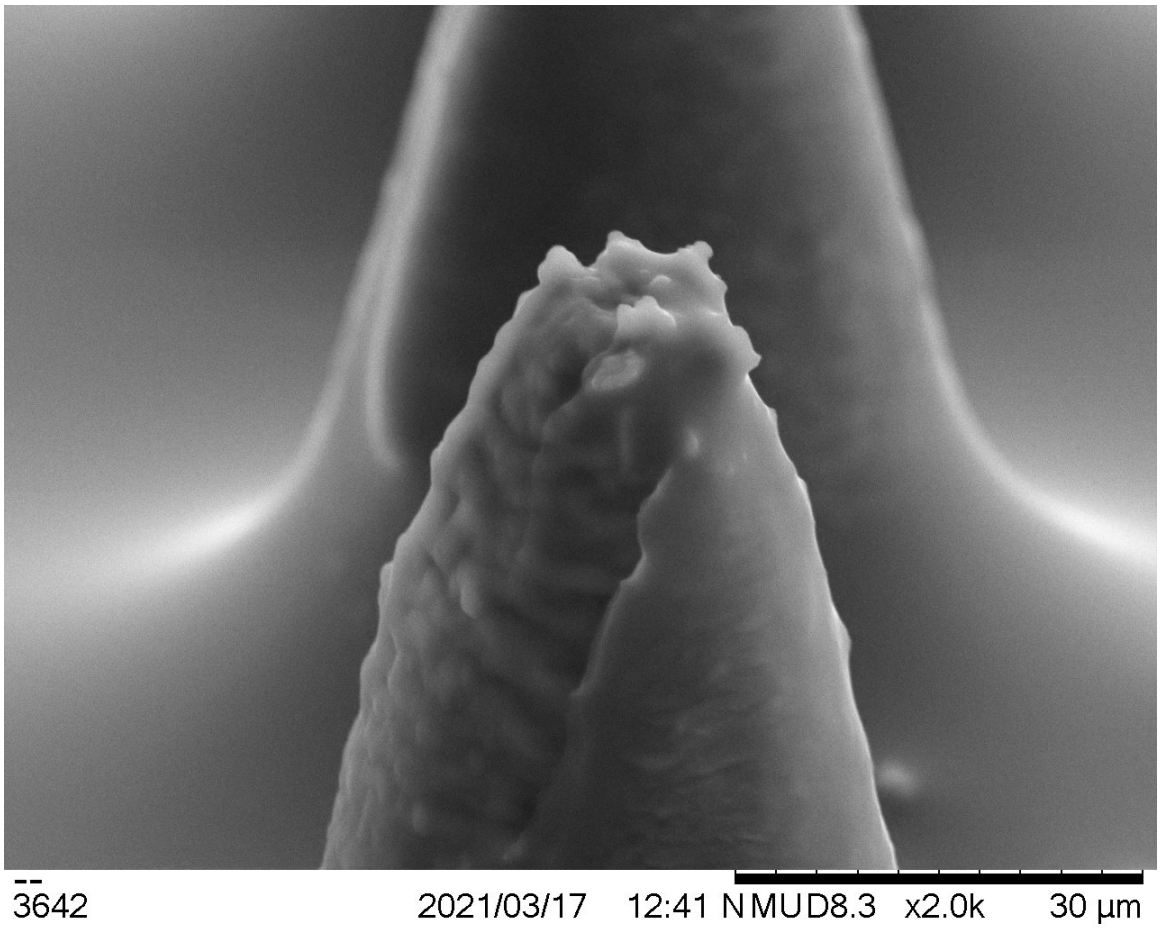

Figure 2-17: SEM image of an emitter tip that appears to have suffered electrochemical wear.

phenomenon, but best practices have been adopted to help prevent the reactions from occurring altogether or to move the reactions to a location that will not result in damage to emitter tips, as discussed in section 1.3.2 and studied extensively by Brikner [4, 5]. The strategies utilized to prevent electrochemical wear for the silicon thrusters include the use of a porous carbon distal electrode and polarity alternation at a frequency sufficient to prevent saturation of the EDL. Anecdotally, these strategies appear to effectively prevent electrochemical wear, as it was an infrequently observed failure mechanism.

In addition to electrochemical reactions, it may be relevant to study neutral chemical reactions of ionic liquids with pure silicon or with dopants in silicon. While direct evidence of such reactions has not been observed, the possibility and severity of these

types of reactions have not been analyzed or studied, and they should therefore be addressed in future work.

2.3 Direct Thrust Measurement

Measurement of thrust is one of the most critical yet difficult aspects of characterizing thrusters for space propulsion, as demand for smallsat-scale propulsion systems has necessitated the development of thrust stands capable of measuring force at the µN level, which requires extremely sensitive and carefully designed instruments. In laboratory settings, thrust from electric propulsion devices is typically measured using pendulum-based thrust stands [58], which measure force by tracking the motion of a pendulum in response to forces or torques delivered by a thruster. Several groups have developed and used pendulum-based thrust stands to directly measure thrust of electrospray, colloid, and FEEP thrusters. In the early 2000s Busek [18] and NASA JPL [72] built torsional thrust stands capable of resolving thrust below the µN level. Later versions of these same thrust stands were used by Busek in 2008 during the development of the Colloid Micro Newton Thruster (CMNT) that flew on the LISA Pathfinder mission [27] and by Legge and Lozano in 2011 to characterize one of the first generations of ionic liquid electrospray thrusters based on porous emitter arrays [37].

Pendulum thrust stands carry many disadvantages. Noise is introduced as a result of the thrust stand being fixed to its environment, and extremely small displacements need to be resolved with great accuracy. The latter issue is often mitigated by the use of null-type thrust stands, which through closed-loop control apply an equal and opposite force on the thruster to keep it fixed in place. While systems that keep the thruster motionless help to alleviate errors caused by movement of the thruster, environmental noise remains a factor, and additional uncertainty is introduced in the restoration force and control system.

Courtney in 2016 used a sensitive mass balance to directly measure thrust of an ionic liquid electrospray system, and the results were compared to indirect thrust

measurements calculated from time of flight mass spectrometry [15]. Alternative instruments have been developed to isolate the thrust stand from its environment to decrease the influence of random errors on thrust measurements. One such instrument is a magnetically-levitated thrust balance where a test vehicle is magnetically levitated in order to provide one friction-free rotational degree of freedom [50]. Thrusters can then be used to produce torques on the test vehicle, and by measuring the resulting change in rotation of the test vehicle the thrust can be inferred [48]. The ultra-dense silicon electrospray thrusters were tested on the magnetically-levitated thrust stand to verify their performance.

2.3.1 Magnetically Levitated Thrust Stand

The magnetically levitated thrust stand (MagLev) in the SPL was designed by Fernando Mier-Hicks and SPL personnel in the 2010s. Its advantages of being contact-free and having 360 degrees of rotational freedom around one axis permit direct thrust measurements with extremely high measurement resolution and allow for more complex thruster tests in addition to direct thrust measurements, including precise angular control experiments [49].

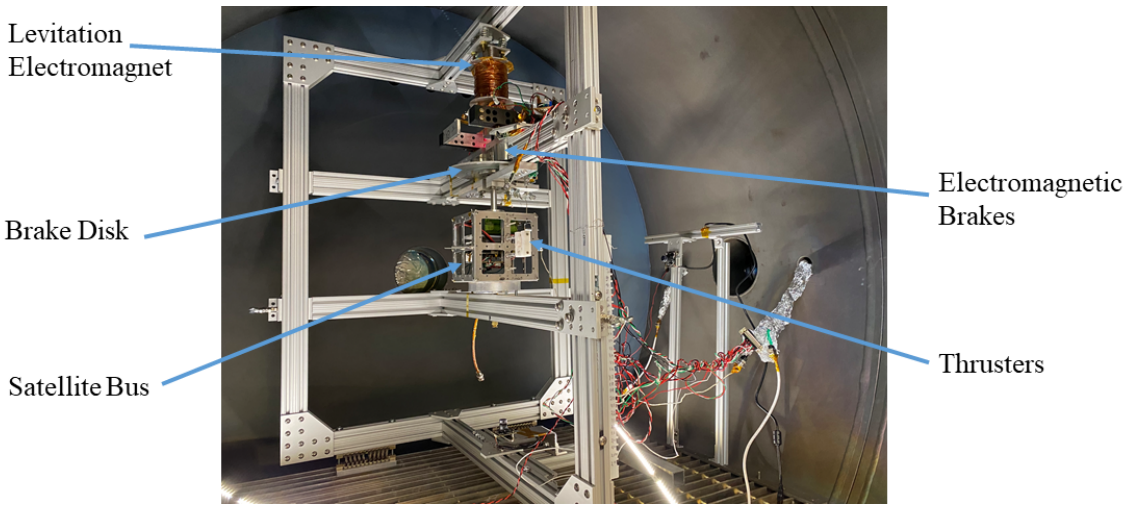

Figure 2-18: Image of the MagLev thrust stand inside the AstroVac vacuum chamber in the SPL.

An image of MagLev with some of the critical components highlighted is shown in

figure 2-18. The thrust stand is comprised of an external structure that is fixed inside a vacuum chamber and a levitated structure that is suspended using magnetic forces within the fixed structure. The fixed structure contains the majority of the electronics, and contact-free actuators and sensors required for MagLev to operate. It also houses the command and telemetry streams that are routed through the chamber wall to a computer for remote operation. The primary component of the levitated structure is a 13 cm cubic satellite structure with a dedicated power system, on-board computer, and propulsion power processing unit (PPU). The test thrusters are mounted to the satellite structure such that they produce torque about the satellite's center vertical axis. Attached to the satellite and therefore part of the levitated structure are several components such as conducting disks, permanent magnets, and optical sensor flags that allow the levitated structure to interact with the fixed structure with making physical contact.

Stable levitation is achieved by interaction of a permanent magnet on the levitated structure and an electromagnet on the fixed structure. An optical sensor detects the vertical position of the satellite relative to its stable levitation point, and a PID controller uses the vertical position sensor feedback to control the current through the electromagnet to hold the satellite position steady within 10 µm of the levitation setpoint. The fixed structure houses two additional electromagnets which, when activated, generate eddy currents in a conducting disk on the levitated structure, thus acting as an electromagnetic brake.

MagLev's on-board PPU is capable of controlling up to four thrusters at once. It is comprised of a printed circuit board (PCB) that houses microcontrollers, power electronics, and sensor circuits necessary to operate electrospray thrusters. Adjustable high-voltage amplifiers can generate emitter potentials up to 1500 V. While electromechanical relays on the PPU allow the operator to switch between several different electrical configuration, the nominal operation mode involves operating thrusters in pairs, with the two thrusters in each pair emitting current of equal magnitude but opposite polarity. This mode of operation maintains electrical neutrality of the satellite bus, which is a critical consideration for MagLev since the satellite is elec-

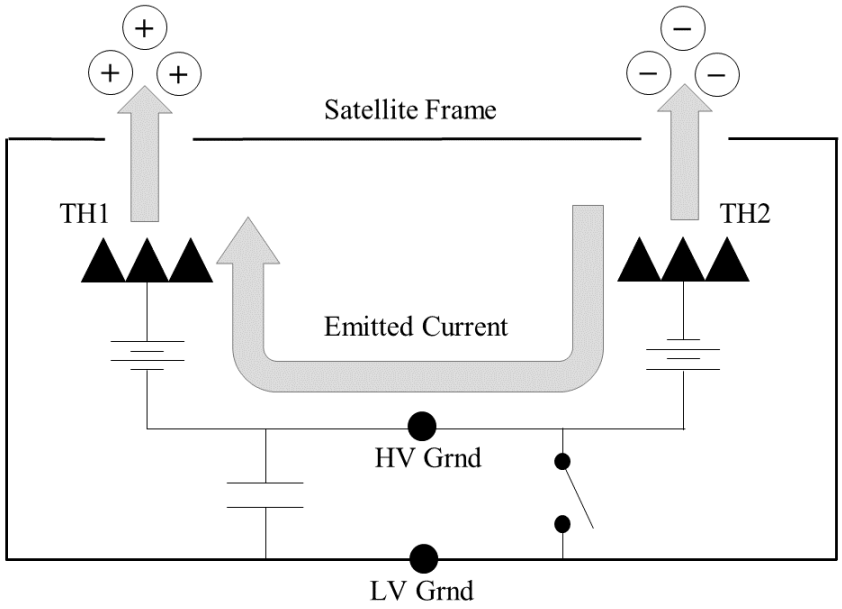

Figure 2-19: Conceptual schematic of the power processing unit (PPU) used to control a pair of thrusters TH1 and TH2 on the MagLev thrust stand.

trically isolated from the external facilities during operation. If the net current out of the satellite deviates from zero, the satellite bus will charge at a rate dependent on the satellite's self capacitance. If the satellite is allowed to charge to large potentials, emitted ions can be attracted back to the satellite, negating the thrust and potentially damaging satellite components and electronics. The thruster pair's currents are constrained to be equal and opposite by connecting their emitters in series and galvanically isolating the high-voltage thruster circuit from the low-voltage PPU electronics, as shown in figure 2-19. Such a configuration ensures that the magnitude of current that flows through both thrusters is equal.

The most critical measurement during a direct thrust measurement on MagLev is the satellite's angular position, because thrust is inferred directly from the response of the satellite's angular position. Angular position is measured using a webcam-based optical sensor mounted underneath the levitated structure. Without making physical contact, the webcam views a fiducial pattern printed on the bottom face of the satellite, and software is used to interpret the pattern and calculate the angular position relative to an arbitrary zero. An example of interpretation of the fiducial

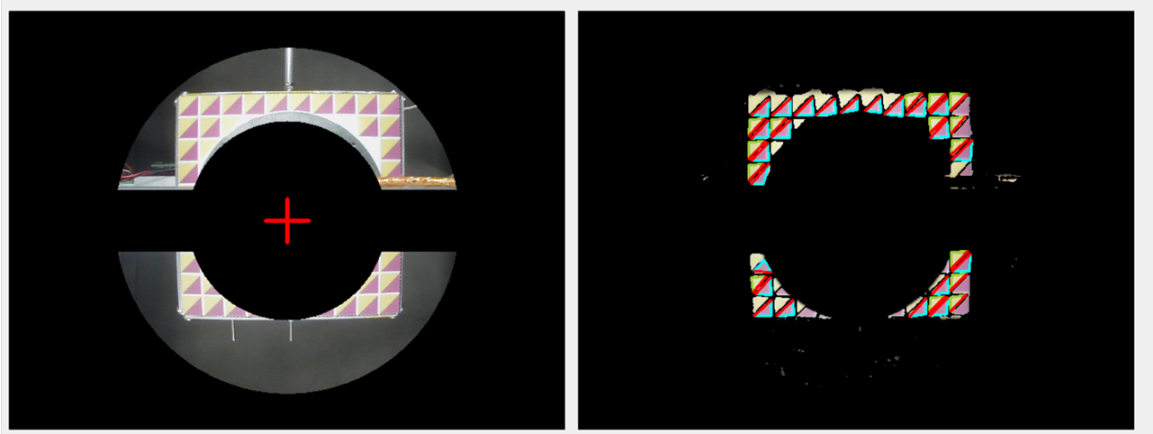

Figure 2-20: Fiducial pattern printed on the bottom of the MagLev test satellite (left) with the software processing the pattern to compute the angular position (right).

pattern by the MagLev software is shown in figure 2-20.

2.3.2 Measurement Principles

A thrust measurement is taken on MagLev by starting with the satellite at rest or in a small oscillation. The satellite oscillates when levitating due to imperfections in the structure of the magnetic field inside the vacuum chamber that interact with the permanent magnet on the levitated structure in a way that causes undamped oscillation. The MagLev fixed structure is equipped with two pairs of Helmholtz coils to negate the effects of the magnetic disturbance and minimize the frequency of the oscillations, but some level of oscillation typically persists. More details regarding the nature and mitigation of these oscillations can be found in [47].

With the satellite at an approximate rest, the thrusters are turned on in unison and with equal but opposite current. The expected response is an angular acceleration, α, of the satellite dependent on the thrust, F, moment of inertia, J, and moment arm of the thruster torque, L. The moment arms and moment of inertia are measured prior to testing. An illustration of each of these parameters on the MagLev satellite is shown in figure 2-21. The equation of motion can be written as

$$J\alpha = F_1 L_1 + F_2 L_2 \tag{2.29}$$

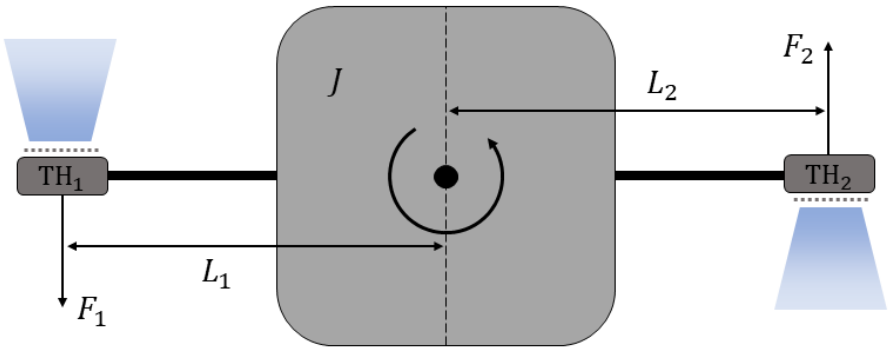

Figure 2-21: Top-down diagrammatic view of the MagLev satellite with thrusters firing to impart a torque around the central axis and rotate the satellite counter-clockwise.

Since L_1 and L_2 are design parameters, they can be made equal so that equation 2.29 simplifies to

$$F_{tot} = \frac{J\alpha}{L} \tag{2.30}$$

where F_{tot} is the combined force of the two thrusters, $F_{tot} = F_1 + F_2$, and $L = L_1 = L_2$. Angular acceleration is determined from the measured angular position. Average angular acceleration and therefore average thrust can be determined over a long firing period, or for sufficiently smooth data instantaneous thrust can be determined at each point in time.

2.3.3 Experimental Results

A pair of 729-tip, 127-µm-pitch thrusters was used for the direct thruster measurement. Each thruster was supplied with 10 µL of EMI-BF_4 via wicks placed on the back of the emitters, and a porous carbon distal electrode made electrical contact between the propellant and the high voltage supply on the PPU. Prior to the experiment, the vacuum chamber was pumped to $< 5 \times 10^{-5}$ Torr using the combined pumping of Edwards Brooks OB-400 and CT-10 cryopumps. During pumpdown, the satellite is levitated so that any undesired motion remaining from the initiation of the levitated is slowly dampened over time, resulting in a satellite experiencing pure

rotation about its central axis at the start of the test.

Immediately prior to firing the thrusters, the Helmholtz coils are calibrated to minimize the frequency and amplitude of oscillations. When the oscillations are minimized and the satellite has reached a stable state, the thrusters are commanded to fire at a prescribed voltage. Though the voltage is the parameter that is controlled, the constraint on the thruster circuit discussed in section 2.3.1 causes the emitted currents to equalize (but in opposite polarities) while the actual potential difference across the thruster electrodes adjusts itself to satisfy the constraint. In this way, if the two thrusters are not identical in their emission characteristics, the thruster with the shallower current-voltage curve will limit the pair. For example, if it is desired to maximize thrust by applying the maximum voltage allowable on the PPU, the weaker thruster will emit its highest current at that maximum voltage while the stronger thruster emits the same current but at a lower voltage.

During the experiment, the thrusters were fired continuously for 30 minutes, increasing the angular velocity of the satellite from 0 to approximately 3.5 $^\circ\,\mathrm{s}^{-1}$. The shape of the angular velocity profile suggests that the acceleration experienced by the satellite can be attributed directly to the torque induced by the thrusters.

Figure 2-22 shows the the measured angular position data, which was discretely differentiated to produce the angular velocity profile. A quadratic polynomial was fit to the position data, and the derivative of the quadratic model was used to approximate the angular velocity. The polynomial fits agreed very well with the measured data. The slope of the linear angular velocity model was used to estimate α, which was found to be $\alpha = 0.035$ mrad s^{-2}. The moment of inertia was measured prior to the test using a trifilar pendulum, and the moment arm was measured using a ruler, resulting in $J = 0.00557$ kg m^2 and $L = 13.1$ cm. Using equation 2.30, the total thrust was calculated to be $F = 1.5$ µN. Throughout the test interval, the thrusters were operating at an emission current of approximately 5.4 µA per thruster. It is not possible to separate the thrust contributions from the individual thrusters without additional information and data points. Since it is known that both thrusters emit equal current magnitudes, it can be safely assumed that the two thrusts will be com-

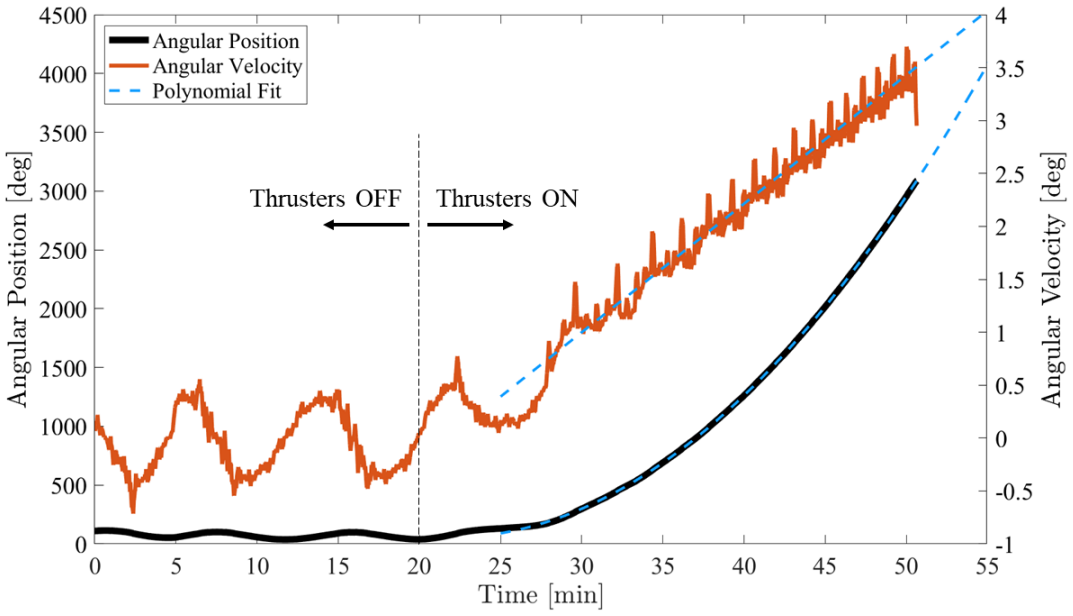

Figure 2-22: Angular position and velocity data acquired during the direct thrust measurement test of the ultra-dense silicon thrusters.

parable. However, differences in the firing voltage and the beam composition of the two thrusters nearly eliminates the possibility of the two thrusts being exactly equal. Under the approximation that the two thrusts are similar, each thruster contributed about 0.75 µN.

Based on TOF measurements, the expected thrust at a current of 5.4 µA and voltages on the order of 1 kV is approximately 0.6 µN, which is in good agreement with the measured thrust. The small disagreement between the measured and expected results can be attributed to several factors. First, the TOF measurement and direct thrust measurement were taken independently in different facilities and using different equipment at different points in time. In fact, it was necessary to reassemble and refill the thrusters in between measurements, which can inadvertently change their properties. Therefore, the usefulness of the comparison between the two values is limited to orders of magnitude. In the future, work will be done to perform TOF and direct thrust measurements in close proximity, which will enable more appropriate comparisons between the two. Also, since it is necessary to fire two thrusters simultaneously on the MagLev thruster stand so that pure torque is produced and

spacecraft neutrality is maintained, future work will address the problem of properly differentiating the two thrust contributions, which is possible to do with a carefully selected pair of thrusters and sufficient information about their characteristics. A methodology for separating the thrust contributions is proposed and tested in [29].

Chapter 3

Thermally Augmented Electrospray Thruster

Instead of, or in addition to, packing more emitter tips into arrays, thrust density can be increased by augmenting the current emitted per tip. Here, a methodology is introduced to augment electrospray performance by efficiently controlling the temperature of the thruster chip and therefore the liquid propellant. This approach would enable increases in thrust beyond what is possible today, increases and/or the ability to modulate thrust-to-power, which establishes how fast maneuvers can be performed and how much propellant is consumed given the spacecraft power resources, and improved lifetime and overall operational stability by allowing materials with pore sizes much smaller than what is used today. In addition, controlling the thruster temperature introduces a novel throttling scheme in which the temperature is controlled by relatively simple low-voltage electronics to reach desired operational parameters.

A simplified implementation of this concept is illustrated in Figure 3-1, where a temperature sensor S_T is added for closed-loop operation. The temperature of the thruster head will be proportional to the power dissipated by the heater, which is given by,

$$P_L = \frac{V_H^2}{(2R + R_L)^2} R_L \tag{3.1}$$

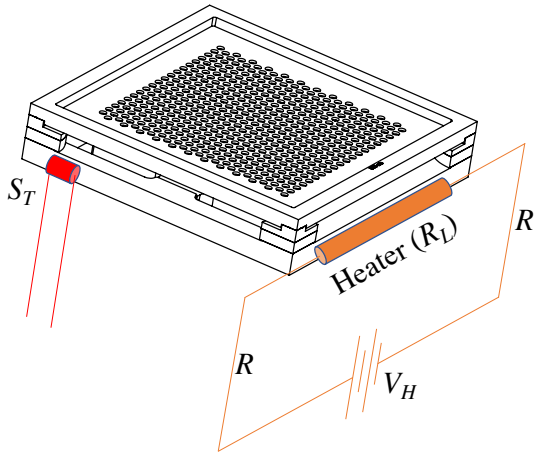

Figure 3-1: Schematic of an electrospray (iEPS) thruster chip with a heater and temperature sensor (S_T)

It can easily be proved that the highest dissipated power will be achieved when the heater resistance is equal to the overall line resistance, or $R_L = 2R$. If, for instance, the heater is connected via 36 gauge (AWG) wire, and each lead is about 2 cm long, then the optimal heater resistance should be $R_L \approx 0.06\ \Omega$. The heater efficiency is given by,

$$\eta = \frac{P_L}{P_h} = \frac{R_L}{2R + R_L} \tag{3.2}$$

P_h is the power required by the heating system. It can be seen that $\eta = 0.5$ for the case of maximum power dissipated by the heater. Higher efficiencies would require operating in conditions where less power is dissipated in the heater, so a compromise is required.

It has been shown through modeling of a notional heating system and of the electrospray emission characteristics that thrust, and therefore the thrust-to-power ratio, of an electrospray thruster can be increased under a constant power constraint by decreasing the firing potential and reinvesting that power into heating of the thruster. The proposed method leverages the idea that under currently-understood scaling laws for electrospray emission, the increase in emitted current afforded by the decrease in propellant viscosity exceeds the decrease in current caused by the decrease in firing potential. Therefore, a heated electrospray thruster can operate at a higher

thrust than an unheated thruster for the same total consumed power.

3.1 Applications and Scenarios

To illustrate this concept, a model is created by considering the modification of an electrospray thruster by affixing a resistive heater to thruster chip near the extraction site, as shown in Figure 3-1. In this way, only the portion of the propellant that is near the extraction site will be heated, rather than the entire propellant tank. This highlights another key advantage of this approach, as microfabricated electrospray thrusters have very low thermal mass, such that minimal power is required to raise their temperature. This can be compared to other forms of electric propulsion that require propellant heating. For instance, field-emission electric propulsion (FEEP) thrusters using liquid metals as their propellant. The temperature of these metals must reach their melting point to be able to flow at all. Therefore, FEEP thrusters must consume power heating the entire propellant tank to allow for the flow of liquid metal into their emitters. This can come at a high penalty, especially for missions with large ΔV requirements that necessitate large propellant tanks. For example, indium is the most common metal used in these thrusters. The melting point of indium is relatively low for a metal (about 157°C), but still requires significant power diverted to the heater to achieve the required temperature. On the other hand, most ionic liquids supercool and are therefore liquid even at temperatures as lows as -80°C, so they can flow freely through the propellant tank to the emitters at practically any operating temperature. Only the relatively small mass of the thruster head is heated to decrease the viscosity of the propellant flowing through it and allow for higher magnitudes of emitted current. This is because the porous material in the thruster chip is not only the material that supports the emitter tips, but also the flow network that establishes flow resistance.

Through electrohydrodynamic simulations, relationships relating emitted current I_{em} to properties of the ionic liquid propellant and composition of the ion beam have

been developed. One such relationship is given in equation 3.3 [8].

$$I_{em} \propto \frac{(q/m)\rho}{Z_{tot}} \tag{3.3}$$

where q/m is the average charge-to-mass ratio of the emitted species, ρ is the propellant mass density, and Z_{tot} is the total hydraulic impedance between the propellant reservoir and the emission site. The hydraulic impedance is directly proportional to propellant viscosity, μ, which is a strong function of temperature. While the dependence of ρ on temperature is less significant, variations as large as 5% between 0°C and 100°C have been measured [63]. To account for the variations of both μ and ρ, we will model the behavior in terms of kinematic viscosity, $\nu = \mu/\rho$. The effect of temperature on q/m is not sufficiently characterized, but for this analysis it will be assumed constant. Thus, equation 3.3 can be rewritten as,

$$I_{em}\nu = A_0(V) \tag{3.4}$$

where A_0 is a constant that depends on firing potential V only. The value of the constant A_0 can be determined experimentally by observing the emitted current of the device at a known temperature and viscosity. The dependence of viscosity on temperature is well known for most common ionic liquids. Here, we consider the ionic liquid 1-ethyl-3-methylimidazolium tetrafluoroborate (EMI-BF_4), as it is well characterized for use as a propellant in electrospray thrusters.

3.1.1 Thermal Modeling

To model the power required to increase the temperature of the propellant near the extraction site, a lumped parameter system in steady-state is considered. In other words, the increase in temperature of the thruster is related to the power input to the heater through a parameter G_{th} and a heater efficiency η. The parameter G_{th} can be thought of as an overall thermal conductance in $\mathrm{W\,K^{-1}}$ between the heated thruster head and some constant-temperature thermal reservoir, in this case the structure on

which the thruster head is mounted on (usually the tank itself). The power into the system is supplied by the heater, $P_{in} = \eta P_h$, and the power out of the system is the product of the thermal conductance to the environment and the change in temperature, $P_{out} = G_{th}\Delta T$. At steady state, $P_{in} = P_{out}$, so

$$P_h = \frac{G_{th}\Delta T}{\eta} \tag{3.5}$$

While the lumped parameter system is a simplistic way to view the complex thermal network that exists within the thruster, it is a good approximation of the behavior at steady-state, and G_{th} values for different configurations are relatively easy to determine experimentally. It is also important to note that heat transfer by convection or radiation are not considered, as their contributions should be negligibly small, especially in vacuum.

From equation 3.5, it is evident that the power required to heat the propellant to some temperature is minimized when G_{th} is low (representing a well-thermally-insulated thruster) and η is high (representing a high-efficiency heater system). It should be noted that equation 3.5 does not consider time needed to heat the system, as it is assumed that the system has reached a steady condition. The assumption that the time required to reach steady state is small is valid for a low-thermal-mass system. This again highlights the utility of needing to heat only the thruster head rather than the entire propellant tank, because the power required to raise the propellant temperature and the time needed to reach that temperature is independent of the total propellant mass in the tank.

Transient Analysis

While heating times are expected to be small, it is worthwhile to consider the transient behavior of the thermal control system. One possible disadvantage to using temperature rather than voltage to modulate thrust is the time needed to reach change the operating condition. The magnitude of an applied voltage can be changed over time scales on the order of milliseconds using modern electronics, while we would

expect the time needed to reach a new temperature to be orders of magnitude higher. Whether this difference in modulation time is significant depends on the particular use case. To determine the time scale of the temperature changes, we can relax the steady-state assumption and model the heat input to the thruster. When considering time transients, the thermal mass (also known as the thermal or heat capacity) of the system becomes relevant. The heat capacity C_{th} has SI units $\mathrm{J\,kg^{-1}\,K^{-1}}$ and is related to the net heat input Q and a rise in temperature ΔT by,

$$C_{th} = \frac{Q}{\Delta T} \tag{3.6}$$

In this context, C_{th} is another parameter that lumps together a network of several parts comprised of different materials and geometries. C_{th} is the combined effect of the heat capacities for each part, which could be computed theoretically using the known volume, densities, and specific heats of each part. However, due to the complexity and occasional nonuniformity of some of the parts, C_{th} is more accurately determined by experiment. Rearranging equation 3.6 and taking a time derivative gives,

$$\frac{dQ}{dt} = P_{in} - P_{out} = \eta P_h - G_{th}\Delta T = C_{th}\frac{d\Delta T}{dt} \tag{3.7}$$

where $P_{in} = \eta P_h$ is the input power from the heater and $P_{out} = G_{th}\Delta T$ is the power loss due to conduction to the environment. We see that the result is a first order inhomogeneous ordinary differential equation in ΔT,

$$\frac{d\Delta T}{dt} + \frac{G_{th}}{C_{th}}\Delta T = \frac{\eta P_h}{C_{th}} \tag{3.8}$$

the solution for which is,

$$\Delta T(t) = \Delta T_0 e^{-t/\tau} + \frac{\eta P_h}{G_{th}}(1 - e^{-t/\tau}) \tag{3.9}$$

where τ is a thermal time constant that is equal to ratio of thermal capacity to thermal conductance:

$$\tau = \frac{C_{th}}{G_{th}} \tag{3.10}$$

With equations 3.5 through 3.10, a framework has been established for experimentally determining the two lumped parameters G_{th} and C_{th} that define the notional thermal system. First, the power required to hold the thruster head in steady state at some level above room temperature can be measured, forming a relationship between P_h and ΔT from which G_{th} can be inferred using equation 3.5. Next, with P_h fixed the transient temperature rise or fall of the thruster can be tracked and fitted to equation 3.9, giving an estimate for τ and subsequently C_{th}. It would be desirable to perform the latter experiment during a cooling period ($P_h = 0$) so that the homogeneous solution, which is simpler to fit to experimental data, can be used. The exponential fit to the cooling profile gives an estimate for τ, and with knowledge of G_{th} already obtained from the steady-state experiments, C_{th} can be directly estimated using equation 3.10.

3.1.2 Analytical Approximations

Though the relationships between current, voltage, and temperature for an electrospray thruster are complex and best determined experimentally, it is possible to derive analytical approximations by making several key assumptions. First, we model the viscosity of an ionic liquid as Arrhenius equation, as is done by Liu [38]:

$$\nu(T) = \nu_\infty \exp\left(-\frac{E_a}{RT}\right) \tag{3.11}$$

where ν_∞ is the viscosity at infinite temperature, R is the ideal gas constant, and E_a is an apparent activation energy. Fitting experimental viscosity data published by Shamsipur [63] to equation 3.11 yields $\nu_\infty = 1.46 \times 10^{-9}\ \mathrm{m^2\,s^{-1}}$ and $E_a = -2.42 \times 10^4\ \mathrm{J\,mol^{-1}}$.

The current-voltage characteristic of the thruster is more difficult to accurately fit to a simple model. The IV curve for an electrospray thruster most closely resembles that of a forward bias diode. The Shockley diode equation is commonly used to model

the IV characteristics of a diode:

$$I(V) = I_0\Big[\exp\left(V/V_0\right) - 1\Big] \tag{3.12}$$

where I_0 is a reverse saturation current and V_0 a thermal voltage. For an electrospray, I_0 and V_0 do not have physical meanings the way they do in diodes, and they are rather just model coefficients. For large forward biases, the second term in equation 3.12 is often neglected, and the IV curve can be modeled as

$$I(V) = I_0 \exp\left(\frac{V - V_s}{V_0}\right) \tag{3.13}$$

where V_s is a parameter that is introduced to the model to represent the effective startup voltage of the thruster, i.e. the voltage at which the current becomes significant. Inclusion of V_s does not change the model mathematically, but it allows us to represent $I(V)$ in terms of physical values in addition to model coefficients. Current-voltage data was acquired for a test electrospray thruster at room temperature and fit to equation 3.13, yielding $I_0 = 12.7$ µA, $V_0 = 107.2$ V, and $V_s = 765.5$ V. The sample IV curve used to estimate these parameters and the fitted exponential model is shown in figure 3-2. Equations 3.11 and 3.13 give approximations for the complex behavior of both the propellant properties as a function of temperature and the current output as a function of voltage, and we can use them to derive analytical approximations for thruster performance metrics.

Consider the relationship in equation 3.4, where A_0 is an empirical constant for a given thruster and depends on voltage only. Using the analytical approximations above, the dependency of A_0 on voltage can be expressed explicitly by multiplying the emitted current at some condition by the viscosity at the same condition.

$$A_0(V) = \nu_0 I_0 \exp\left(\frac{V - V_s}{V_0}\right) \tag{3.14}$$

where ν_0 is the kinematic viscosity at the reference condition at which I_0 and V_0 are measured. In principle, ν_0, I_0, and V_0 can be taken at any condition, but it is reasonable to use room temperature as the standard condition.

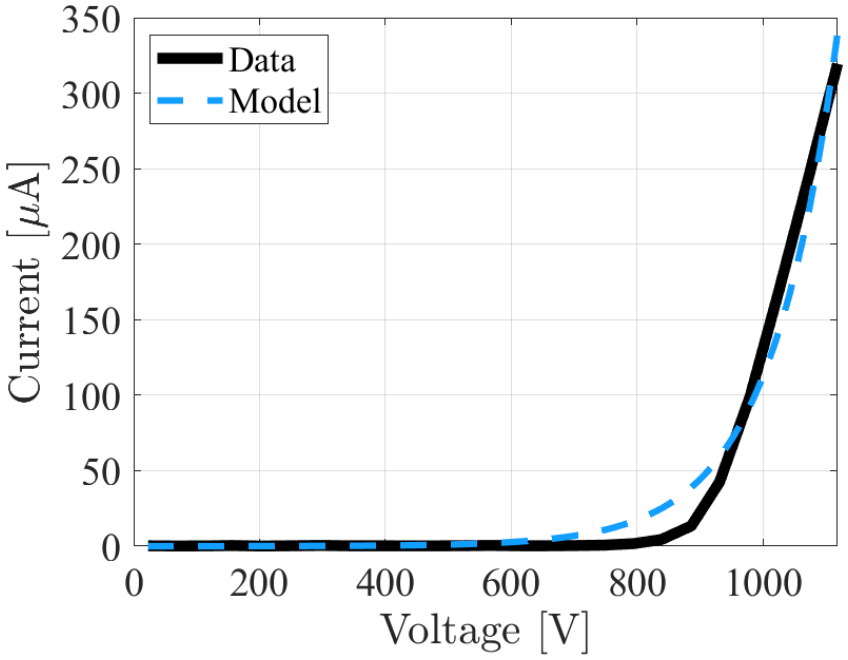

Figure 3-2: Current-Voltage of an iEPS electrospray thruster at room temperature in the positive firing mode fitted via the method of least squares to equation 3.13.

Now, equations 3.4, 3.11, and 3.14 can be combined to arrive at an expression for emitted current as a function of both temperature and voltage in terms of parameters measured at the reference state and other coefficients:

$$I_{em}(V,T) = \frac{A(V)}{\nu(T)} = \frac{\nu_0 I_0 \exp\left(\frac{V-V_s}{V_0}\right)}{\nu_\infty \exp\left(-\frac{E_a}{RT}\right)} = \frac{\nu_0 I_0}{\nu_\infty} \exp\left(\frac{V-V_s}{V_0} + \frac{E_a}{RT}\right) \tag{3.15}$$

Thruster power is $P_t = V I_{em}$, and heater power P_h is given by equation 3.5. The total electrical power consumed by the propulsion system is $P = P_t + P_h$. Thrust F in terms of current, voltage, and other thruster constants is derived in section 2.2.1, and the result is summarized in equation 2.18. We define a thruster coefficient $\phi = \sqrt{2/(q/m)}$ that is assumed to be constant for a given thruster. With these assumptions, analytical approximations for P and F can be written:

$$P(V,T) = P_t + P_h = \frac{\nu_0 I_0}{\nu_\infty} V \exp\left(\frac{V - V_s}{V_0} + \frac{E_a}{RT}\right) + \frac{G_{th}(T - T_0)}{\eta} \tag{3.16}$$

$$F(V,T) = \phi \frac{\nu_0 I_0}{\nu_\infty} \sqrt{V} \exp\left(\frac{V - V_s}{V_0} + \frac{E_a}{RT}\right) \tag{3.17}$$

Dual-Grid Approximations

A dual-grid electrospray is one that uses two extractor grids in series, each of which can be biased individually with respect to the emitter. In such a configuration, the potential difference between the emitter and the first (upstream) grid, called the extraction voltage V_e, controls the electric field seen at the emission site and therefore determines the magnitude of the current extracted from the thruster. Meanwhile, the potential difference between the emitter and the second (downstream) grid, called the acceleration voltage V_a, controls the net potential difference through which ions are accelerated and therefore determines the exhaust velocity. In this way, thrust and specific impulse can be controlled separately via independent control of V_e and V_a.

Dual-grid systems have several benefits, all of which will not be discussed here, but of particular interest is the manner in which they can be applied to a heated electrospray concept. Thermal control is another mechanism by which thrust can be modified without changing specific impulse. With at least three independent variables (V_e, V_a, and T), the complete trade space for this configuration is quite large and complex, but it is worthwhile to form analytical approximations for the quantities of interest in the dual-grid case as was done for the single-grid case. This amounts to changing V in equations 3.15 through 3.17 to either V_e or V_a, depending on the voltage that correctly controls each part of the equations. The results are given in equations 3.18 through 3.20

$$I_{em,dual}(V_e,T) = \frac{\nu_0 I_0}{\nu_\infty} \exp\left(\frac{V_e - V_s}{V_0} + \frac{E_a}{RT}\right) \tag{3.18}$$

Table 3.1: Model coefficients fitted for the analytical approximations of the thermally augmented electrospray thruster

Coefficient	Fitted Value	Units
ν_∞	1.46×10^9	$\mathrm{m^2\,s^{-1}}$
ν_0	2.50×10^5	$\mathrm{m^2\,s^{-1}}$
E_a	-2.42×10^4	$\mathrm{J\,mol^{-1}}$
I_0	12.7	µA
V_s	765.5	V
V_0	107.2	V
ϕ	0.00224	$\sqrt{\mathrm{kg\,C^{-1}}}$

$$P_{dual}(V_e, T) = \frac{\nu_0 I_0}{\nu_\infty} V_e \exp\left(\frac{V_e - V_s}{V_0} + \frac{E_a}{RT}\right) + \frac{G_{th}(T - T_0)}{\eta} \tag{3.19}$$

$$F_{dual}(V_e, V_a, T) = \phi \frac{\nu_0 I_0}{\nu_\infty} \sqrt{V_a} \exp\left(\frac{V_e - V_s}{V_0} + \frac{E_a}{RT}\right) \tag{3.20}$$

It is noteworthy that $I_{em,dual}$ and P_{dual} are have no dependence on V_a because the emission current consumes power through V_e only. However, F_{dual} is a function of both V_e and V_a (as well as T) because both the magnitude of the current and the speed of the exhausted ions contribute to thrust. It is clear from even these simple approximations that there is a very wide range of scenarios that can be analyzed to evaluate the impact of using thermal augmentation in an electrospray propulsion system. A small selection of such scenarios is analyzed in the following sections to give an overview of the types of operations and optimizations that are enabled.

3.1.3 Operating under Constrained Power

The first scenario considered is that when the propulsion system is constrained to operate at or below some maximum total power P. This power can be divided between the heater power P_h and the thruster power $P_t = VI_{em}$ such that $P = P_h + P_t$. If it is desired to use all available power, then in the unheated case the thruster would be operating at the firing potential V such that $P = P_t = VI_{em}$. However, if power

is removed from the thruster by decreasing V, and that newly available power is reinvested into heating the thruster, we can evaluate the impact on overall thruster performance parameters like thrust F and thrust-to-power ratio F/P, a measure of how efficiently the propulsion system converts electrical power to thrust.

Computations for all scenarios were performed assuming the average charge-to-mass ratio in the ion beam is $q/m = 400\ \mathrm{C\,g^{-1}}$. The analytical relationships derived in section 3.1.2 were used to compute the relationships between F/P, I_{sp}, and T at a constant total power of 2 W. The relationships were computed for a range of G_{th}, since the thermal conductance can be considered a design parameter. A complete list of the correlation coefficients used in the analytical approximations is given in table 3.1.

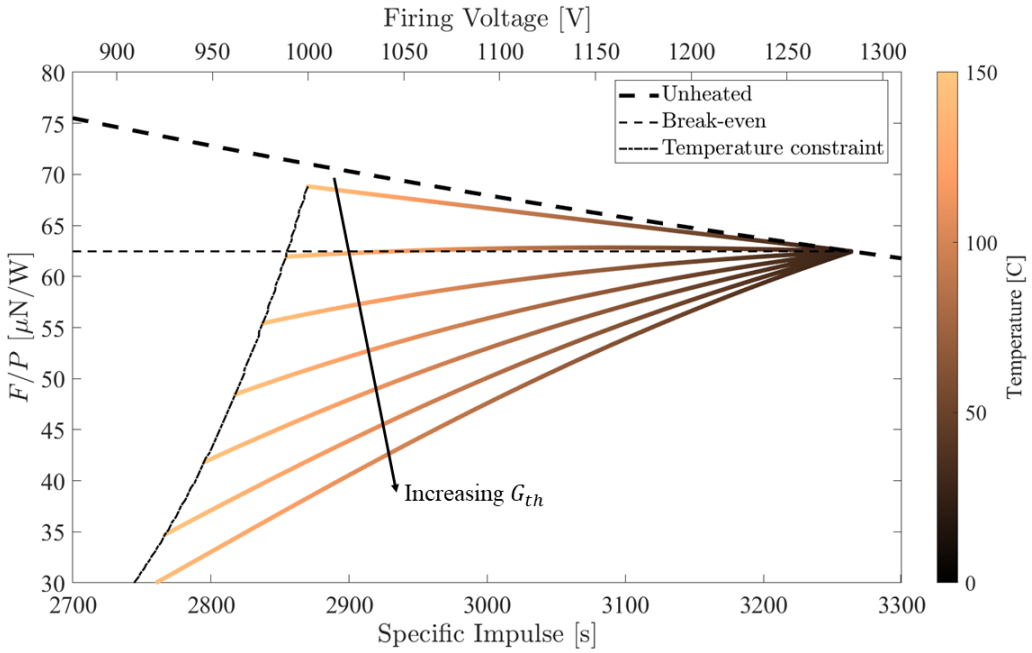

Figure 3-3: Thrust-to-Power ratio achievable over a range of firing potentials for a constrained total power of 2 W. Different curves represent different values of the lumped conductance G_{th}, where $0.0005 \leq G_{th} \leq 0.01$ in $\mathrm{W\,K^{-1}}$ and with the top curve representing the lowest G_{th}. Temperature was constrained to 150°C.

Figure 3-3 illustrates that for a properly designed heating system, i.e. a sufficiently small G_{th}, the maximum thrust-to-power ratio achievable for a given power constraint is not at the maximum firing potential V where all power is invested directly into

the thruster. Instead, by decreasing the voltage and investing the excess power into heating the thruster, more current can be extracted at the lower voltage, and the net effect is an increase in thrust. On the other hand, figure 3-3 reveals that for a poorly designed heating system with insufficient insulation, no such advantage is gained. It becomes clear that care must be taken in the design of the thermal control system to ensure that $G_{th} < G_{crit}$, the critical conductance at which the maximized F/P matches the unheated condition. The model predicts a critical conductance of $G_{crit} \approx 0.0027$ W K^{-1}.

For electric propulsion systems like the iEPS, the negligible heat dissipation of the thruster itself and the chemical inertness of the propellants used allows for widespread use of plastics and other low-thermal-conductivity materials in the construction of the thruster and tank. These materials offer good thermal insulation between the thruster head where the heater system will be operating and an external structure, a satellite bus for example, whose temperature can vary significantly. Regardless, it is evident that thermally controlling the thruster enables active modulation of F/P, even if an increase is not attainable due to a relatively large G_{th}. The ability to modulate F/P in real time is particularly useful for satellites that perform a wide range of maneuvers, such as small satellite swarms flying in formation, because different maneuvers may be optimized at different F/P levels.

3.1.4 Thrust Modulation by Thermal Control

A particularly interesting application of a heated electrospray thruster is the modulation of current, and therefore thrust, output by adjusting the emitter *temperature* rather than the emitter *voltage*. Such a throttling scheme could greatly simplify the electronics required to operate electrosprays. The adjustable high-voltage amplifiers used to modulate emitter voltage are bulky, expensive, and suboptimal from an electrical efficiency perspective. In addition, complex networks of large, heavy electromechanical relays are required to control and switch the high-voltage electronics. If adjustable voltage amplifiers can be replaced by fixed-voltage modules, the electronics can be miniaturized, simplified, and optimized.

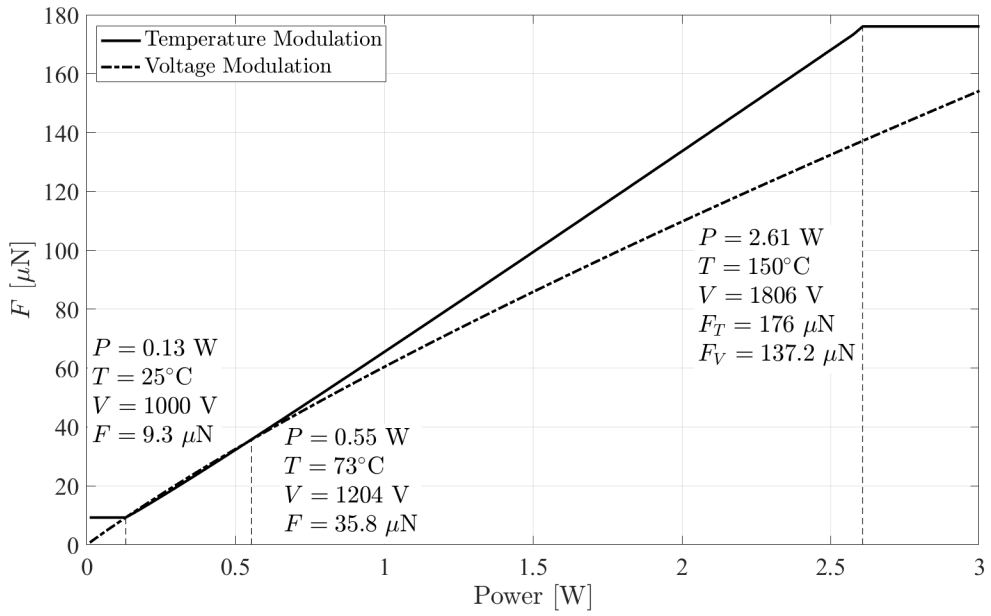

Figure 3-4: Comparison of output thrust at a range of input powers for temperature modulation at fixed voltage $V_0 = 1000$V (solid line) and voltage modulation at fixed temperature $T_0 = 25°$C (dashed line). The temperature was constrained to 150°C and the thermal conductance was assumed to be $G_{th} = 0.001$ W K^{-1}.

To evaluate the effectiveness of using temperature modulation to control thrust, consider operating an electrospray at a fixed emitter voltage. For thruster designs utilizing a single extractor grid responsible for both extraction and acceleration of ions, fixing emitter voltage also fixed specific impulse, assuming the average charge-to-mass ratio of the ion beam does not change. Because there are natural limits to the range of temperatures that can be used, temperature modulation introduces an operational window that may be narrow compared to the available window using voltage modulation. Assuming the thruster is equipped only with a heating system and is therefore without cooling capability, the thruster cannot be operated below ambient temperature, setting the lower bound to the throttle window. The upper temperature limit is driven primarily by the operating ranges of the propellants and materials used in thruster fabrication. For instance, EMI-BF_4 decomposes at approximately 292°C [70]. The PEEK and PTFE plastic components used in the iEPS tank assembly have glass transition temperatures near 143 and 114°C, respectively, and they melt entirely at temperatures in excess of 300°C. While these materials are often used at

temperatures in excess of their glass transition temperatures, maintaining the material properties of the tank components is critical in ionic liquid electrospray systems to prevent leakage of ionic liquid, which can not only deplete propellant supply but also permanently damage electronic components. For these analyses, the thruster temperature limit is set at 150°C.

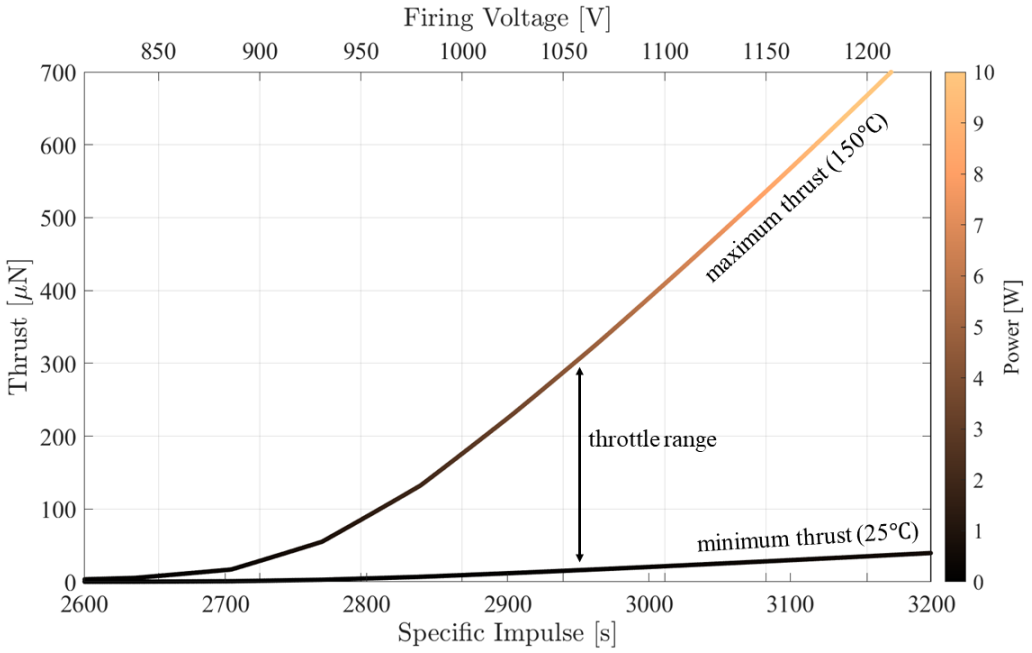

Figure 3-5: Bounds of the throttling range of a temperature-modulated thruster at a range of firing voltages and a temperature limit of 150°C.

Figure 3-4 compares the throttling range of two notional thrusters using temperature modulation and voltage modulation to control thrust. It is noteworthy that inside the operational window, the thrust versus power profiles of the two schemes are similar, with temperature modulation being slightly more efficient in thrust-to-power at higher power levels. However, figure 3-4 also shows the restrictions introduced by the temperature constraints in the temperature modulation case. With the thruster unable to operate below 25°C or above 150°C, only a limited range of thrust and power values are achievable.

A simple way to adjust and increase the throttle window for temperature modulation is to change the nominal emitter voltage. Specifically, by increasing the fixed emitter voltage the minimum, maximum, and range of available thrust levels all in-

crease. This relationship is illustrated in figure 3-5. It is evident that by using thermal augmentation at high firing voltages, very large maximum thrust levels are achievable. However, operating at these high thrust levels comes at the cost of increased power, with the higher ranges requiring upwards of 10 W of input power, much larger than power levels typically available for systems of this size. Nonetheless, even the extreme operating points are in principle attainable for a thruster that satisfies these assumptions and obeys these models.

3.1.5 Dual-Grid Electrospray Thruster

Ion thrusters, including electrosprays, that utilize two in-series grids for ion extraction and acceleration can control thrust and specific impulse independently. Several operational modes are enabled by such an architecture. For instance, it becomes possible to extract small currents with a low extraction voltage V_e but accelerate the current to high exit velocities with a high acceleration voltage V_a, enabling low-thrust, high-specific-impulse operation that can be useful for highly efficient and precise attitude control. On the opposite end of the spectrum, a high-thrust, low-specific-impulse mode is enabled, which may be optimal for certain mission profiles or maneuvers. Most importantly, the dual-grid architecture enables operation at an infinite number of combinations of thrust and specific impulse in between the two extremes, allowing unprecedented agility and real-time optimization of maneuvers.

Introducing thermal augmentation to dual-grid electrospray further expands the range of possible modes, since temperature becomes a third control parameters that can independently modulate the magnitude of emitted current and other thruster performance metrics without changing specific impulse. Figure 3-6 shows an example of one application, focusing on a scenario in which a power constraint is imposed on the propulsion system, and T, V_e, and V_a are adjusted to modulate the output and performance metrics of the thruster without changing the total power consumed. It can be seen that for a system with the assumed properties, F/P increases monotonically over the relevant temperature range. The returns diminish due to the viscosity of EMI-BF_4 reaching a terminal value at high temperature, and for very high temper-

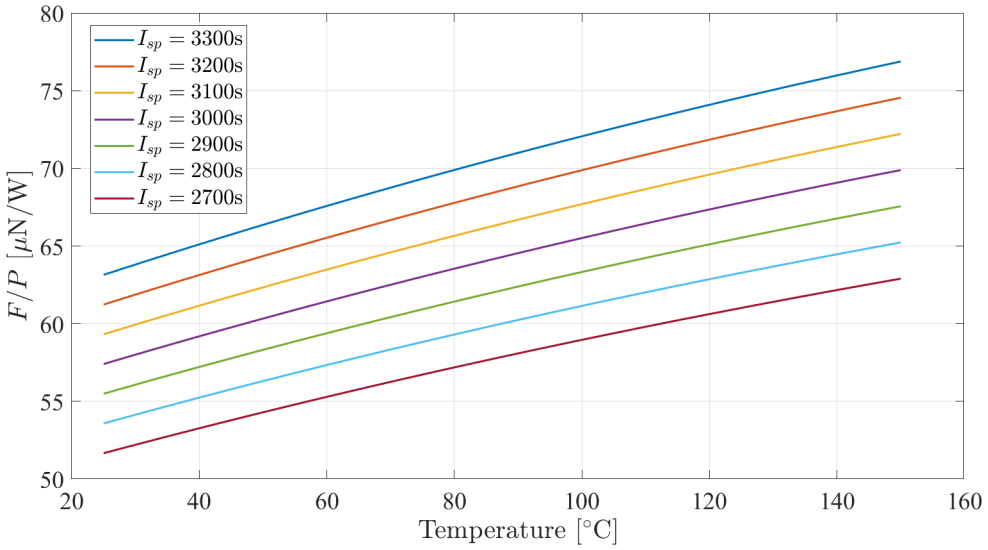

Figure 3-6: Thrust-to-power ratio of a dual-grid electrospray thruster operating at a fixed power of 2 W as a function of temperature for different values of specific impulse. The thermal conduction parameter was assumed to be $G_{th} = 0.001$ W K^{-1}.

ature F/P reaches a maximum and begins to degrade. The location of the maximum F/P is dependent on the properties of the system, such as G_{th} and the coefficients used to model the electrospray emission behavior.

It is interesting to note that the trade space illustrated in figure 3-6 is unique to a dual-grid system, since in a single-grid system fixing two of the power, specific impulse, and temperature fixes the the third. However, in a dual-grid system all three can be adjusted independently, resulting in a wide and continuous range of F/P over which the thruster can operate, enabling a unique method by which it is possible to adjust thruster parameters in real time and choose the optimum operation mode for a given maneuver.

Shown here are just some of the many possibilities that are enabled by a thermally augmented electrospray system, illustrating at a basic level how investing power to heat the thruster can serve to change, and in some special cases improve, thruster performance metrics. Additional scenarios and analyses that focus on different thruster parameters or performance metrics will be driven by use case, but from the above analyses alone it is clear that thermal augmentation has the potential to greatly ex-

pand the range of use cases in which electrospray thrusters are a viable propulsion system for several classes of space systems.

3.2 Heated Electrospray Testing

To test the hypothesis, a closed-loop temperature control system compatible with the iEPS electrospray thruster was designed. A resistive heater sized to deliver the appropriate amount of power and a resistance temperature detector (RTD) were bonded to the frame of an iEPS thruster. The heater system was used to fire the thruster at various steady-state temperature conditions.

The goals of the experimental validation were multiple. First, it was desired to evaluate the heater system itself, primarily characterizing the relationship between heater power and temperature rise, which involves experimental determination of the thermal conductance G_{th} from equation 3.5. Second, we sought to experimentally verify the relationship described in equation 3.4. If the scaling law holds and it is valid to assume that the beam composition remains constant with temperature, then the current magnitude as a function of temperature is highly predictable.

3.2.1 Heater System Design

The heater and RTD are bonded to the 1 mm edge of the silicon thruster frame using Masterbond Supreme 11AOHT-LO epoxy, a thermally conducting but electrically insulating adhesive that is ASTM E595 compliant (low outgassing). Sufficient electrical insulation between the frame and the heater system components is crucial because the thruster frame is biased to voltages in excess of 1 kV during operation. The McPherson model [46] was used to estimate the dielectric breakdown field of the epoxy based on its known dielectric constant, and epoxy barriers were applied to sustain at least 5 kV, more than twice the expected level.

A 150 Ω ruthenium oxide thick film resistor with a maximum power dissipation of 3 W was used as the heater load, and a 100 Ω platinum RTD was used as the temperature sensor. 28 AWG copper wire made up the electrical lines, the total resistance of

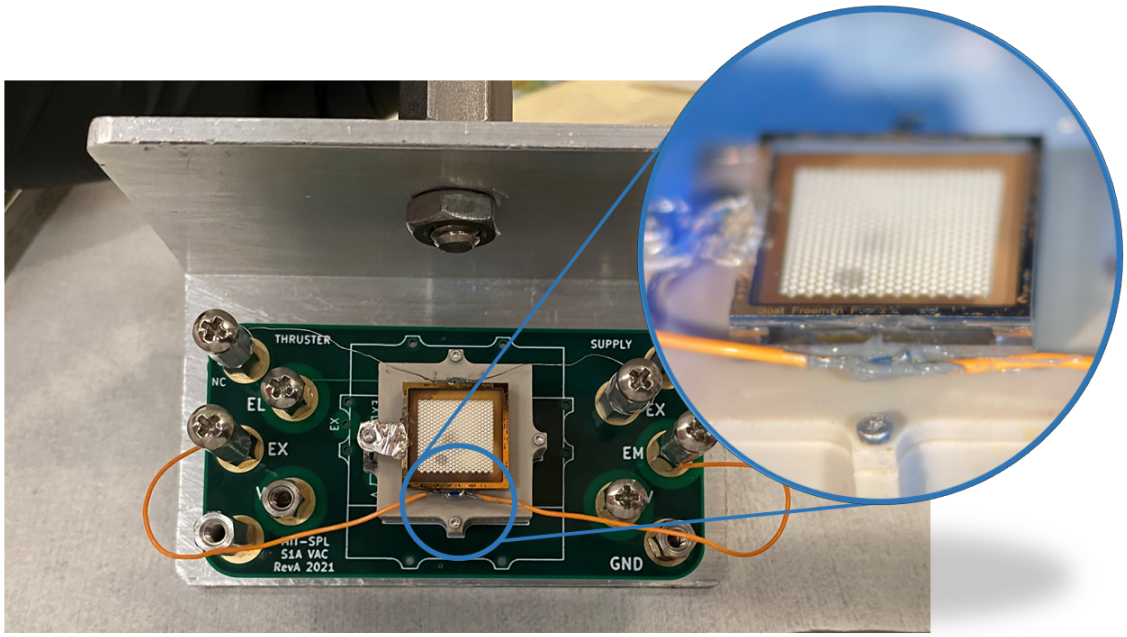

Figure 3-7: Heater bonded to emitter frame of an iEPS thruster

which impacts the heater efficiency. The temperature of the thruster is controlled using an Arduino-based PID controller with the RTD temperature measurement as the process variable and a pulse width modulation (PWM) signal as the control variable. The PWM signal switches a MOSFET that opens and closes the heater circuit at the controlled duty cycle. A 12 V DC power supply is used to power the heater circuit, allowing for a maximum heater power at 100% duty cycle of $P_{max} = V^2/R = 0.96$ W.

3.2.2 Experimental Results

The first experiments were performed simply to determine the relevant parameters of the thruster and heater system, primarily G_{th}, C_{th}, and η. Heater efficiency η can be measured directly by taking high-resolution resistance measurements. A Keithley 6514 electrometer was used to precisely measure the line and load resistances. Heating experiments were performed in a vacuum chamber at pressures below 1×10^{-2} Torr, and thruster firing experiments were performed in the same chamber at pressures below 5×10^{-6} Torr.

To determine G_{th}, the system was placed in the vacuum chamber and the tem-

perature was controlled to various setpoints between 30°C and 105°C (which, for this system, was approximately the steady-state temperature T_{max} at maximum heater power P_{max}) while the power required to maintain the temperature was tracked. Power was calculated as the maximum heater power multiplied by the duty cycle output by the PID. The system was allowed to dwell in steady-state at each setpoint for at least several minutes to allow all variables to stabilize, and the average power over the interval was considered to be the heater power required to maintain the temperature. The relationship between heater power and steady-state temperature is shown in figure 3-8.

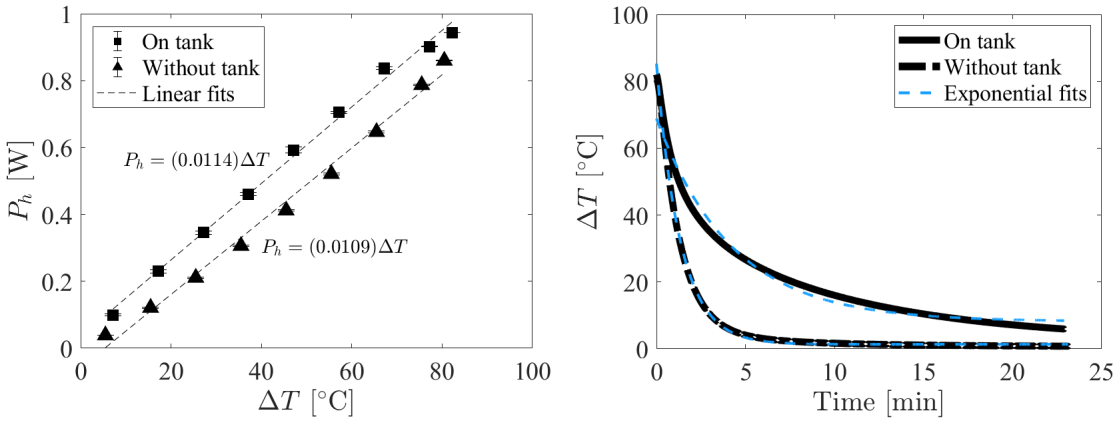

Figure 3-8: (left) Heater power required to raise the temperature of the thruster by a range of amounts above the ambient temperature for a thruster mounted on a tank and a thruster floating in vacuum. (right) Cooling profiles of the same two thrusters.

Two main sources of conduction to the ambient environment were identified: conduction through the propellant tank and conduction though the electrical connections themselves. To isolate the effects of these two sources and inform the optimal design for the heater system, an equivalent heating experiment was performed using a thruster that was not mounted to a tank and was instead suspended in vacuum by the electrical connections. In this configuration. Conduction to the environment is possible only through the electrical connections. The heater power and temperature results are shown alongside the data from the thruster on a tank in figure 3-8. Per equation 3.5, the slope of the P_h versus ΔT relationship provides an estimate for G_{th}, and it is evident that there was not a significant difference in the G_{th} estimate

between the thruster mounted on a tank and the floating thruster, with the average of the two being $G_{th} = 0.0112$.

Several conclusions can be drawn from the above observation: (1) the heat loss due to conduction seems to be dominated by the electrical connections. Since the tank materials are thermally insulating plastics, such an observation is not surprising. (2) It is possible to tailor G_{th} via selection of wire materials and sizes. For example, 28 AWG copper wire was used to make the electrical connections to the heater, temperature sensor, and extractor electrode. Each of the five connections used approximately 2 cm of wire. Given the diameter of 28 AWG, $d = 0.321$ mm, and the thermal conductivity of copper, $\kappa \approx 400\ \mathrm{W\,m^{-1}\,K^{-1}}$, the expected thermal conductivity would be $G = 5\kappa A/L \approx 0.00813\ \mathrm{W\,K^{-1}}$, which would represent the majority of the value found experimentally using the data in figure 3-8. Therefore, to decrease G_{th}, which is desired to minimize the required power investment for a given ΔT, it may be desirable to use wire of smaller diameter or to select non-traditional materials that have poorer thermal conductivities but maintain high electrical conductivities for electrical connections. Unfortunately, very few of such materials exist, since there is a well-known correlation between electrical and thermal conductivity. However, a metal such as titanium may be a good choice, since both its thermal and electrical conductivities are approximately 5% that of copper. Optimization of the heater system will be addressed in future work.

To determine the effective thermal mass, C_{th}, of the system, it was brought its maximum steady-state temperature, approximately 105°C for both thrusters, and allowed to cool under zero heater power to ambient temperature. With $P_h = 0$, the transient behavior of ΔT given in equation 3.9 simplifies to

$$\Delta T(t) = \Delta T_0 e^{-t/\tau} \tag{3.21}$$

which is simple to fit to experimental data using the method of least squares. The experimental cooling curves and exponential fits are shown in figure 3-8, yielding estimates for the thermal time constant of $\tau = 254$ seconds and $\tau = 80$ seconds for

Table 3.2: Experimentally determined thruster and heater system thermal parameters.

η	> 0.99
G_{th}	$0.0112\ \mathrm{W\,K^{-1}}$
C_{th}	$2.9\ \mathrm{J\,K^{-1}}$
τ	254 s

the thruster on a tank and without a tank, respectively. Clearly, there is a large discrepancy in the time constant between the two configurations. Since it has been shown that the two configurations have similar G_{th}, the discrepancy must come from a difference in C_{th}, the effective thermal mass of the system. Using equation 3.10, the effective thermal mass of the two configurations is estimated to be $C_{th} = 2.9\ \mathrm{J\,K^{-1}}$ and $C_{th} = 0.88\ \mathrm{J\,K^{-1}}$, respectively. The thermal mass can be interpreted as the amount of *energy* required to raise the temperature by 1 degree, while the thermal conductance is the *power* required to *maintain* that temperature. One interpretation of the discrepancy is that when the thruster is mounted to a tank, some of the heat input is used to raise the temperature of the tank components near the interface between the thruster and the tank rather than the thruster head alone, raising the effective thermal mass. In this way, it is evident that both the insulation of the thruster-tank interfaces and the electrical connections are relevant and should be designed to minimize both C_{th} and G_{th}.

After determining the thermal characteristics of the heated thruster system, the thruster was fired at a range of temperature setpoints to determine the accuracy of the predicted relationship between temperature and emitted current (equation 3.4). The propellant tank was filled with 0.4 mL of EMI-BF_4 prior to the start of testing. Filling operations were performed in a CO_2 environment. The thruster was fired initially at room temperature ($T_0 = 25°\mathrm{C}$) to establish the baseline against which to compare the emission characteristics at elevated temperatures. The firing voltage was selected such that the emitted current was close to its nominal level for an iEPS thruster. For this thruster, the room temperature operating point was approximately 135 µA at a firing

voltage of 860 V. The kinematic viscosity of EMI-BF_4 at 25°C is $\nu_0 = 25$ mm^2 s^{-1}, so the value of the constant A_0 is calculated to be $A_0(860\text{V}) = I_e m \nu_0 = 3.38 \times 10^{-9}$ A mm^2 s^{-1}. The heater system was then used to control the temperature of the thruster chip at various elevated setpoints, and the thruster was allowed to fire, without adjusting the firing voltage, at the setpoint for several minutes to allow both the temperature and current levels to settle. The polarity of the emitter potential was reversed every 30 seconds to avoid electrochemical effects. The current values reported are averages of the positive and negative modes over a given interval.

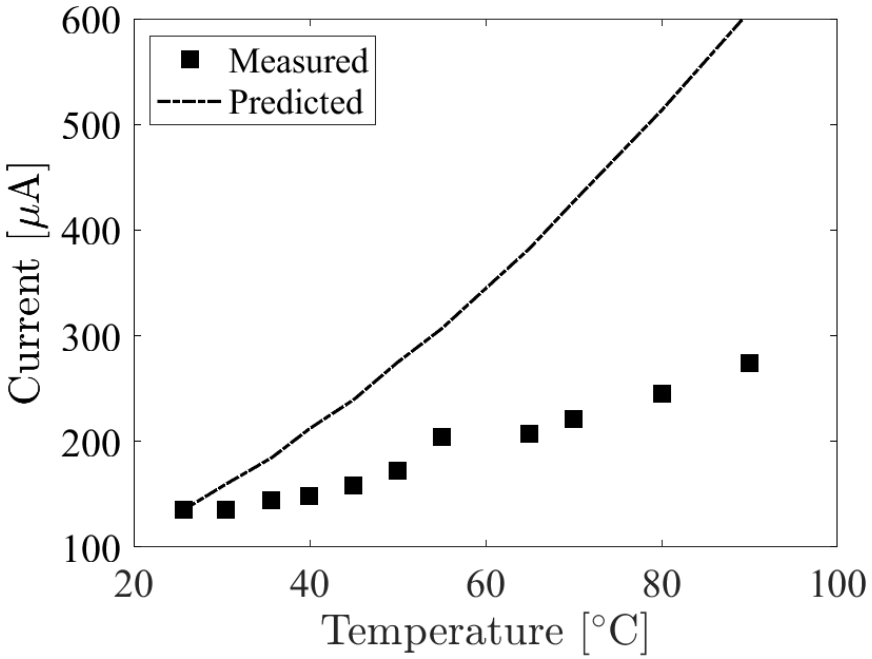

Figure 3-9: Measured and expected emission current as a function of temperature.

Figure 3-9 shows the measured current at temperature setpoints ranging between 25 and 90°C alongside the expected current based on the room temperature current and the temperature dependence of viscosity. It is evident that measured current is well below the predicted curve. While emitted current would have been expected to increase to values as large at 600 µA at 90°C, the actual current was closer to 300 µA. It is believed that these are the first data acquired from an integrated ionic liquid electrospray propulsion system at elevated temperatures. Previous studies on the effect of temperature on ILIS, such as those done by Lozano [41], were performed

using single tungsten emitters. Full porous glass emitter arrays, due to their different mechanism of propellant transport, different emitter tip size scale, different method of emitter biasing, and other factors, exhibit different behaviors than single metal tips in certain scenarios.

Several factors may contribute to the disagreement observed in figure 3-9. First, it is assumed in equation 3.4 that the average charge-to-mass ratio of the ion beam is unchanged as both temperature and current are increased. In reality, there may be some dependence of q/m on temperature, which should be addressed in future work. For example, time of flight mass spectrometry measurements taken for a thruster firing at different temperature setpoints could reveal such a dependence. In addition, insufficient heat transfer between the thruster frame and the propellant flowing through the porous glass emitter may result in an overestimation of the true propellant temperature. Methods for passively increasing heat flow between the components in the thruster head could be implemented, including selecting thermally conductive adhesives for interfaces and minimizing heat loss to other components, such as the tank and propellant bulk. Alternatively, the propellant temperature could, in principle, be probed more directly such that the feedback to the thermal control system would be representative of the true propellant temperature near the thruster head.

Another factor that was not controlled in these experiments is contamination of the propellant, including during assembly/filling by atmospheric water vapor or during operation by decomposition products. In the former case, the hygroscopic nature EMI-BF_4 results in absorption of water from humid air, which may impact the viscosity-temperature relationship of the propellant, changing the expected current-temperature relationship in an unknown way. The latter case may result from unexpectedly strong thermal gradients across the thruster between the heater and temperature sensor, potentially causing local temperatures near the heater to exceed the thermal decomposition temperature of EMI-BF_4. Decomposition products include highly viscous or sometimes solid substances, which would reduce the effective pore size of the emitter and resist flow. Both of these effects can be mitigated, however, by drying the propellant prior to filling and by distributing the heat dissipation around

the perimeter of the thruster to prevent extreme thermal gradients.

All of the above factors, as well as some others not discussed here, may impact the emission characteristics of a thruster at elevated temperatures, and future work shall focus on the isolation of these factors and development of a representative model for the temperature dependence of electrospray emission properties. Regardless, it is evident that active thermal control has a significant impact on the magnitude of current capable of being extracted from an electrospray thruster at a given firing voltage, though the net effect may be milder than expected, pending a more thorough and controlled investigation of a prototypical heated electrospray system. The difference between the measured and expected outputs seen in figure 3-9 impacts the scenarios and relationships discussed in section 3.1, and future work should address the origins of these discrepancies and incorporate them into a more comprehensive model of a thermally augmented electrospray system.

Chapter 4

Conclusions

Here, a preliminary framework is proposed for future improvements to the performance characteristics of ionic liquid electrospray propulsion systems, with thrust density as the driving figure of merit. Two complementary paths are evaluated: decreasing emitter pitch to increase the packing density of emitting tips, and using active thermal control to augment the magnitude of current capable of being emitted from each tip. Benefits and drawbacks exist in both cases, and the two methodologies are not mutually exclusive. Increasing emitter packing density necessitates the use of different materials and more advanced fabrication techniques to create highly complex three-dimensional geometries at the microscopic scale, but it leverages well-understood principles of electrospray physics and is therefore relatively predictable and reliable. Thermal augmentation requires design of an efficient thermal control system and operation of electrospray thrusters under conditions in which their characteristics are poorly understood and unpredictable, but in addition to augmentation of current it enables active modulation of thruster performance metrics and a novel throttling scheme.

In both cases, increasing the thrust density of electrospray thrusters requires increasing the current emitted per unit area, the effects of which are not yet widely understood. Several factors that are typically considered negligible in electrosprays, such as heat dissipation and space charge, may become significant at increased current densities, and the critical point at which phenomena such as these must be consid-

ered is not yet known. For this work to be continued, it is likely necessary to take an in-depth look at the physics of ion emission in electrospray thrusters at the molecular level to better understand the factors that will significantly influence macroscopic thruster performance. The tests performed here serve merely as proofs of concept for the principles and ideas that may lead not only to a better understanding of electrospray thrusters but also improved designs that can potentially have an enormous impact on the market for small spacecraft propulsion.

4.1 Ultra Dense Emitters

Emitter arrays fabricated using grayscale lithography from silicon with pitch as low as 127 µm were tested for the first time as an integrated thruster system with an extractor grid electrode and ionic liquid propellant. Initial performance of the ultra-dense arrays was promising, with evidence of repeatable and stable emission in the pure ionic regime and current levels consistently exceeding 60 µA at voltages on the order of 1 kV.

Several performance characteristics of the ultra-dense silicon thrusters were measured both directly and indirectly using test equipment and diagnostics in the Space Propulsion Laboratory at MIT. Current-voltage measurements, retarding potential analysis, time of flight mass spectrometry, and beam divergence measurements were performed and compiled to obtain an overall view of the preliminary performance and efficiency of the thrusters. Finally, a magnetically levitated thrust stand was used to measure thrust directly.

4.2 Thermal Augmentation

Thermal augmentation was also identified as a method by which thrust density can be increased. Such a methodology would leverage the tendency of the viscosity of liquids to decrease sharply with increased temperature and the understanding that current emitted from an ionic liquid ion source is expected to increase with decreased

viscosity and all other parameters constant. An analytical framework was developed to model the emission characteristics and performance metrics of an electrospray thruster under variable firing voltage and temperature, and several cases were analyzed to illustrate the potential usefulness of a thermally augmented electrospray in a variety of scenarios, including optimizing thrust-to-power ratio under fixed power, using temperature to modulate thrust at fixed voltage, and application of the concept to a dual-grid electrospray thruster.

It was shown that active heating enables modulation of several thruster performance metrics, expanding the potential use cases for electrospray thrusters and enabling real time optimization of orbital maneuvers. In addition, it was seen that for a well designed thermal control system and under a specific set of conditions, thruster performance metrics can be improved, including maximization of thrust-to-power ratio and augmentation of current density.

To demonstrate the concept of thermal augmentation, an active thermal control system was designed and applied to an MIT iEPS electrospray thruster and tested in vacuum. After characterization of the thermal characteristics of the system, the thruster was fired over a range of temperature setpoints, and the thruster current output was observed. It was shown that current magnitude monotonically increases with temperature over the relevant range, proving that thermal augmentation is feasible. However, agreement between the theoretical models and experimental results was not clear, so additional work is to be done to investigate the causes of the discrepancies and inform the models for a thermally augmented electrospray system.

4.3 Future Work

Work to further develop the proofs of concept covered here is necessary to push forward the state of the art in electrospray propulsion. The two systems tested, an ultra dense silicon based electrospray thruster and a thermally augmented electrospray thruster, are prototypes for their respective technologies, and therefore further iteration and development of their designs will yield clearer experimental results.

For instance, it has been proven that the ultra-dense MEMS emitters can emit a pure ion beam and produce measurable thrust, as observed via diagnostic data and demonstrated using a magnetically levitated thrust stand. However, the novel thruster concept is still in development, and its performance characteristics are expected to change as design details, including those having to do with emitter-extractor interfaces and fluid control, are matured.

An immediate next step in the development of the ultra-dense thrusters is to acquire long-duration firing data, which was not able to be obtained up to this point. Long duration data yields information regarding the evolution of the thruster's behavior over time and the maximum lifetime achievable for the thruster. It also enables direct measurements of the average mass flow rate over a firing duration, since propellant mass consumption approaches levels that can be measured using laboratory scales. Firing for long durations (hundreds of hours) requires a propellant tank to store the volume of ionic liquid needed for such a test. The design for the iEPS ionic liquid propellant tank has been extensively tested and qualified for space flight, so development of an interface between the silicon thrusters and the iEPS tank is underway to be able to obtain long duration data. The long term outlook for the silicon thrusters may involve development of a new tank design tailored toward the needs of classes of satellites even smaller than the cubesats for which the iEPS was designed.

Additionally, more direct thrust measurements should be taken for the ultra-dense silicon thrusters, and at different firing conditions (i.e. current levels). Additional data points will yield a better understanding of the thruster characteristics and measurement uncertainty, and it will allow for differentiation of the contributions of individual thrusters from a pair firing on the MagLev thrust stand.

Ultimately, since the ultra-dense silicon thrusters have been demonstrated in the laboratory, it will be beneficial to conduct an on-orbit demonstration of the technology to further develop and qualify the technology. On-orbit demonstrations provide the most reliable data for a thrusters ability to survive the harsh conditions of launch and perform in space. Since a satellite's position can be tracked very accurately, information about the propulsion system's performance can be inferred via measurement

of changes in orbital elements in response to a known thruster command. Similar demonstrations for new propulsion systems are performed frequently, and they are the only way for a technology to graduate to a technology readiness level (TRL) of 9.

The thermally augmented electrospray thruster system is also in a developmental state, with the proof of concept complete and the development of a more reliable and precise system underway. The first prototype utilized easily accessible components and relatively simple assembly methods, but future iterations may focus on optimization of the heater system, either to maximize efficiency or to maximize power through the heater load.

In addition, more comprehensive models should be developed to accurately and repeatably predict the behavior of electrospray thrusters as a function of temperature. A dedicated model for full porous glass emitter arrays does not exist, and models for single nonporous ILIS may have limited applicability that depends on firing conditions and other variables. For example, a better understanding of the changes to the ion beam with temperature should be established, which includes determination of the temperature dependence on parameters like q/m, which has not been studied but could impact the validity of equation 3.4. Investigation into the discrepancies between the simple model derived in this work and the experimental data may also involve more controlled experiments that can isolate the various confounding variables which may influence the experimental results. Examples include accurate knowledge and control of the actual propellant temperature inside the porous emitter and accurate measurement of the propellant's thermophysical properties and their dependences on temperature. All of these, along with additional experimental data, will contribute to a more comprehensive model for electrospray emission.

Bibliography

[1] Monika Auweter-Kurtz and H. Kurtz. High thrust density electric propulsion for heavy payload in-space transportation. *European Space Agency, (Special Publication) ESA SP*, 555:126, 09 2004.

[2] Natalya Bailey and Raleigh Werner. Electrospray-a powerful third option for electric satellite propulsion an accion systems perspective. *SatMagazine*, Feb 2017.

[3] Alexander C. L. Bost. Materials for small-scale space propulsion systems. Master's thesis, Massachusetts Institute of Technology, Cambridge, MA, June 2017.

[4] Natalya Brikner and Paulo C. Lozano. The role of upstream distal electrodes in mitigating electrochemical degradation of ionic liquid ion sources. *Applied Physics Letters*, 101(19):193504, 2012.

[5] Natalya Anna Brikner. *On the Identification and Mitigation of Life-limiting Mechanisms of Ionic Liquid Ion Sources Envisaged for Propulsion of Microspacecraft*. PhD dissertation, Massachusetts Institute of Technology, February 2015.

[6] Steven Castro and Juan Fernández de la Mora. Effect of tip curvature on ionic emissions from taylor cones of ionic liquids from externally wetted tungsten tips. *Journal of Applied Physics*, 105(3):034903, 2009.

[7] Edgar Y. Choueiri. A critical history of electric propulsion: The first fifty years (1906-1956). In *40th AIAA/ASME/SAE/ASEE Joint Propulsion Conference and Exhibit*, pages AIAA–2004–3334, Fort Lauderdale, July 2004.

[8] Ximo Gallud Cidoncha, Bjarni Ö. Kristinsson, and Paulo C. Lozano. Informing the design of pure-ion electrospray thrusters via simulation of the leaky-dielectric model with charge evaporation. In *36th International Electric Propulsion Conference*, pages IEPC–2019–610, Vienna, Austria, September 2019.

[9] Kenn E. Clark. Survey of electric propulsion capability. *Journal of Spacecraft and Rockets*, 12(11):641–654, 1975.

[10] Chase S. Coffman and Paulo C. Lozano. Direct thrust measurements for a multiplexed borosilicate electrospray source. In *50th AIAA/ASME/SAE/ASEE Joint Propulsion Conference*, pages AIAA–2014–3695, 2014.

[11] Chase S. Coffman, Manuel Martínez-Sánchez, and Paulo C. Lozano. Electrohydrodynamics of an ionic liquid meniscus during evaporation of ions in a regime of high electric field. *Phys. Rev. E*, 99(6):063108, June 2019.

[12] Chase S. Coffman, Louis Perna, Hanqing Li, and Paulo C. Lozano. On the manufacturing and emission characteristics of dielectric electrospray sources. In *49th AIAA/ASME/SAE/ASEE Joint Propulsion Conference*, pages AIAA–2013–4035, 2013.

[13] Daniel Courtney, Hanqing Li, Paulo Lozano, PabloDiaz GomezMaqueo, and Timothy Fedkiw. On the validation of porous nickel as substrate material for electrospray ion propulsion. In *46th AIAA/ASME/SAE/ASEE Joint Propulsion Conference & Exhibit*, pages AIAA–2010–7020, 2010.

[14] Daniel G. Courtney. *Ionic Liquid Ion Source Emitter Arrays Fabricated on Bulk Porous Substrates for Spacecraft Propulsion*. PhD dissertation, Massachusetts Institute of Technology, June 2011.

[15] Daniel G. Courtney, Simon Dandavino, and Herbert Shea. Comparing direct and indirect thrust measurements from passively fed ionic electrospray thrusters. *Journal of Propulsion and Power*, 32(2):392–407, 2016.

[16] Daniel G Courtney, Hanqing Q Li, and Paulo Lozano. Emission measurements from planar arrays of porous ionic liquid ion sources. *Journal of Physics D: Applied Physics*, 45(48):485203, nov 2012.

[17] A. Feyh, F. Laermer, S. Kronmüller, and W. Mokwa. A novel process for the preparation of thick porous silicon layers with very high porosity. *physica status solidi (a)*, 202(8):1597–1601, 2005.

[18] Manuel Gamero-Castaño, Vlad Hruby, and Manuel Martínez-Sánchez. A torsional balance that resolves sub-micro-newton forces. In *27th International Electric Propulsion Conference*, pages IEPC–01–235, Pasadena, USA, 2001.

[19] Tanya Cruz Garza. Optimizing wettability of externally wetted microfabricated silicon electrospray thrusters. Master's thesis, Massachusetts Institute of Technology, Cambridge, MA, January 2007.

[20] Tanya Cruz Garza, Paulo Lozano, Luis F. Velásquez-García, and Manuel Martinez Sanchez. The characterization of silicon wettability and properties of externally wetted microfabricated electrospray thruster arrays. In *29th International Electric Propulsion Conference*, pages IEPC–2005–195, Princeton, USA, November 2005.

[21] Massimo Guarnieri. The unreasonable accuracy of moore's law [historical]. *IEEE Industrial Electronics Magazine*, 10(1):40–43, 2016.

[22] C Guerra-Garcia, D Krejci, and P Lozano. Spatial uniformity of the current emitted by an array of passively fed electrospray porous emitters. *Journal of Physics D: Applied Physics*, 49(11):115503, feb 2016.

[23] M. Hasanuzzaman, A. Rafferty, M. Sajjia, and A.-G. Olabi. Production and treatment of porous glass materials for advanced usage. *Reference Module in Materials Science and Materials Engineering*, Jan 2016.

[24] R. Herino, G. Bomchil, K. Barla, C. Bertrand, and J. L. Ginoux. Porosity and pore size distributions of porous silicon layers. *Journal of The Electrochemical Society*, 134(8):1994–2000, aug 1987.

[25] Francisco J. Higuera. Model of the meniscus of an ionic-liquid ion source. *Physical Review E - Statistical, Nonlinear, and Soft Matter Physics*, 77(2):026308, 2008.

[26] K. Holste, P. Dietz, S. Scharmann, K. Keil, T. Henning, D. Zschätzsch, M. Reitemeyer, B. Nauschütt, F. Kiefer, F. Kunze, J. Zorn, C. Heiliger, N. Joshi, U. Probst, R. Thüringer, C. Volkmar, D. Packan, S. Peterschmitt, K. T. Brinkmann, H.-G. Zaunick, M. H. Thoma, M. Kretschmer, H. J. Leiter, S. Schippers, K. Hannemann, and P. J. Klar. Ion thrusters for electric propulsion: Scientific issues developing a niche technology into a game changer. *Review of Scientific Instruments*, 91(6):061101, 2020.

[27] Vlad Hruby, Douglas Spence, Nathaniel Demmons, Thomas Roy, Eric Ehrbar, Jurg Zwahlen, Roy Martin, John Ziemer, William Connolly, Scott Rhodes, and Warren Tolman. St7-drs colloid thruster system development and performance summary. In *44th AIAA/ASME/SAE/ASEE Joint Propulsion Conference & Exhibit*, pages AIAA–2008–4824, 2008.

[28] Robert G. Jahn. *Physics of Electric Propulsion*, volume 2 of *The Art of Computer Programming*. Dover Publications, Mineola, New York, 2006.

[29] Oliver Jia-Richards, Matthew N. Corrado, and Paulo C. Lozano. Thrust inference for ionic-liquid electrospray thrusters on a magnetically-levitating thrust balance. In *37th International Electric Propulsion Conference*, pages IEPC–2022–208, Cambridge, USA, June 2022.

[30] Oliver Jia-Richards and Paulo Lozano. Analytical framework for staging of space propulsion systems. *Journal of Propulsion and Power*, 36(4):527–534, 2020.

[31] Oliver Jia-Richards, Paulo C. Lozano, David C. Sternberg, Daniel Grebow, and Swati Mohan. Feasibility of a deep-space cubesat mission with a stage-based electrospray propulsion system. In *2020 IEEE Aerospace Conference*, pages 1–10, 2020.

[32] Robert S. Legge Jr., Paulo Lozano, and Manuel Martinez-Sanchez. Fabrication and characterization of porous metal emitters for electrospray thrusters. In *30th International Electric Propulsion Conference*, pages IEPC–2007–145, Florence, Italy, September 2007.

[33] A. Koponen, M. Kataja, and J. Timonen. Permeability and effective porosity of porous media. *Phys. Rev. E*, 56:3319–3325, Sep 1997.

[34] David Krejci and Paulo Lozano. Scalable ionic liquid electrospray thrusters for nanosatellites. In *39th Annual AAS GNC Conference*, pages AAS–16–124, Breckenridge, USA, February 2016.

[35] David Krejci, Fernando Mier-Hicks, Robert Thomas, Thomas Haag, and Paulo Lozano. Emission characteristics of passively fed electrospray microthrusters with propellant reservoirs. *Journal of Spacecraft and Rockets*, 54(2):447–458, 2017.

[36] Renato Krpoun. *Micromachined Electrospray Thrusters for Spacecraft Propulsion.* PhD dissertation, École Polytechnique Fédérale de Lausanne, January 2009.

[37] Robert S. Legge and Paulo C. Lozano. Electrospray propulsion based on emitters microfabricated in porous metals. *Journal of Propulsion and Power*, 27(2):485–495, 2011.

[38] Fengguo Liu, Xiongwei Zhong, Junli Xu, Ali Kamali, and Zhongning Shi. Temperature dependence on density, viscosity, and electrical conductivity of ionic liquid 1-ethyl-3-methylimidazolium fluoride. *Applied Sciences*, 8(3), 2018.

[39] Ignacio G. Loscertales and J. Fernández de la Mora. Experiments on the kinetics of field evaporation of small ions from droplets. *J. Chem. Phys.*, 103(12):5041–5060, 1995.

[40] Paulo Lozano and Manuel Martinez-Sanchez. Efficiency estimation of emi-bf4 ionic liquid electrospray thrusters. In *41st AIAA/ASME/SAE/ASEE Joint Propulsion Conference & Exhibit*, pages AIAA–2005–4388, 2005.

[41] Paulo Lozano and Manuel Martínez Sánchez. Ionic liquid ion sources: characterization of externally wetted emitters. *Journal of Colloid and Interface Science*, 282(2):415–421, 2005.

[42] Paulo C. Lozano. *Studies on the Ion-Droplet Mixed Regime in Colloid Thrusters.* PhD dissertation, Massachusetts Institute of Technology, February 2003.

[43] Paulo C. Lozano, Brian L. Wardle, Padraig Moloney, and Suraj Rawal. Nano-engineered thrusters for the next giant leap in space exploration. *MRS Bulletin*, 40(10):842–849, 2015.

[44] Colleen Marrese-Reading. Microfluidic electrospray propulsion(mep) thruster performance with microfabricated emitter arrays for indium propellant. In *52nd AIAA/SAE/ASEE Joint Propulsion Conference*, pages AIAA–2016–4738, 2016.

[45] Colleen Marrese-Reading and John R. Anderson. Silicon emitter needle and array design for indium electrospray arrays for spacecraft propulsion. In *52nd AIAA/SAE/ASEE Joint Propulsion Conference*, pages AIAA–2016–4547, 2016.

[46] J. McPherson, J. Kim, A. Shanware, H. Mogul, and J. Rodriguez. Proposed universal relationship between dielectric breakdown and dielectric constant. In *Digest. International Electron Devices Meeting,*, pages 633–636, 2002.

[47] Fernando Mier-Hicks. *Spacecraft Charging and Attitude Control Characterization of Electrospray Thrusters on a Magnetically Levitated Testbed*. PhD dissertation, Massachusetts Institute of Technology, February 2017.

[48] Fernando Mier-Hicks and Paulo C. Lozano. Thrust Measurements of Ion Electrospray Thrusters using a CubeSat Compatible Magnetically Levitated Thrust Balance. In *34th International Electric Propulsion Conference*, pages IEPC–2015–148, Hyogo-Kobe, Japan, 2015.

[49] Fernando Mier-Hicks and Paulo C. Lozano. Electrospray thrusters as precise attitude control actuators for small satellites. *Journal of Guidance, Control, and Dynamics*, 40(3):642–649, 2017.

[50] Fernando Mier-Hicks, Louis Perna, Chase Coffman, and Paulo C. Lozano. Characterization of a CubeSat-Compatible Magnetically-Levitated Thrust Balance for Electrospray Propulsion Systems. In *49th AIAA/ASME/SAE/ASEE Joint Propulsion Conference*, pages AIAA–2013–3879, San Jose, USA, 2013.

[51] Catherine E. Miller. *Characterization of ion Cluster fragmentation in ionic liquid ion sources*. PhD dissertation, Massachusetts Institute of Technology, June 2019.

[52] Gordon E. Moore. Cramming more components onto integrated circuits. *Electronics*, 38(8), 1965.

[53] Gordon E. Moore. Progress in digital integrated electronics [technical literaiture, copyright 1975 ieee. reprinted, with permission. technical digest. international electron devices meeting, ieee, 1975, pp. 11-13.]. *IEEE Solid-State Circuits Society Newsletter*, 11(3):36–37, 2006.

[54] Dillon O'Reilly, Georg Herdrich, and Darren F. Kavanagh. Electric propulsion methods for small satellites: A review. *Aerospace*, 8(1), 2021.

[55] M. Paine and S. Gabriel. A micro-fabricated colloidal thruster array. In *37th Joint Propulsion Conference and Exhibit*, pages AIAA–2001–3329, 2001.

[56] M.D. Paine, S. Gabriel, C.G.J. Schabmueller, and A.G.R. Evans. Realisation of very high voltage electrode–nozzle systems for mems. *Sensors and Actuators A: Physical*, 114(1):112–117, 2004.

[57] Elaine M. Petro, Amelia R. Bruno, Paulo C. Lozano, Louis E. Perna, and Dakota S. Freeman. Characterization of the tile electrospray emitters. In *AIAA Propulsion and Energy 2020 Forum*, pages AIAA–2020–3612, August 2020.

[58] James E. Polk, Anthony Pancotti, Thomas Haag, Scott King, Mitchell Walker, Joseph Blakely, and John Ziemer. Recommended Practices in Thrust Measurements. In *33rd International Electric Propulsion Conference*, pages IEPC–2013–440, Washington DC, USA, 2013.

[59] Henry H. Radamson, Huilong Zhu, Zhenhua Wu, Xiaobin He, Hongxiao Lin, Jinbiao Liu, Zhenzhen Kong Jinjuan Xiang, Wenjuan Xiong, Junjie Li, Hushan Cui, Jianfeng Gao, Hong Yang, Yong Du, Buqing Xu, Ben Li, Xuewei Zhao, Jiahan Yu, Yan Dong, and Guilei Wang. State of the art and future perspectives in advanced cmos technology. *Nanomaterials (Basel)*, 10(8):1555, 2020.

[60] I. Romero-Sanz, R. Bocanegra, J. Fernandez de la Mora, and M. Gamero-Castaño. Source of heavy molecular ions based on taylor cones of ionic liquids operating in the pure ion evaporation regime. *Journal of Applied Physics*, 94(5):3599–3605, 2003.

[61] Joseph H. Saleh, Fan Geng, Michelle Ku, and Mitchell L.R. Walker. Electric propulsion reliability: Statistical analysis of on-orbit anomalies and comparative analysis of electric versus chemical propulsion failure rates. *Acta Astronautica*, 139:141–156, July 2017.

[62] Jurriaan Schmitz. State of the art in microfabrication. In *Technology and Instrumentation in Particle Physics 2014*, 2014.

[63] Mojtaba Shamsipur, Ali Akbar Miran Beigi, Mohammad Teymouri, Sayed Mahdi Pourmortazavi, and Mohsen Irandoust. Physical and electrochemical properties of ionic liquids 1-ethyl-3-methylimidazolium tetrafluoroborate, 1-butyl-3-methylimidazolium trifluoromethanesulfonate and 1-butyl-1-methylpyrrolidinium bis(trifluoromethylsulfonyl)imide. *Journal of Molecular Liquids*, 157(1):43–50, 2010.

[64] Noah W. Siegel. Silicon wafer integration of ion electrospray thrusters. Master's thesis, Massachusetts Institute of Technology, Cambridge, MA, May 2020.

[65] Melissa A. Smith, Shaun Berry, Lalitha Parameswaran, Christopher Holtsberg, Noah Siegel, Ronald Lockwood, Michael P. Chrisp, Daniel Freeman, and Mordechai Rothschild. Design, simulation, and fabrication of three-dimensional microsystem components using grayscale photolithography. *Journal of Micro/Nanolithography, MEMS, and MOEMS*, 18(4):1 – 14, 2019.

[66] R. L. Smith and S. D. Collins. Porous silicon formation mechanisms. *Journal of Applied Physics*, 71(8):R1–R22, 1992.

[67] P. Steiner and W. Lang. Micromachining applications of porous silicon. *Thin Solid Films*, 255(1 – 2):52 – 58, 1995.

[68] Geoffrey Ingram Taylor. Disintegration of water drops in an electric field. *Proceedings of the Royal Society of London. Series A. Mathematical and Physical Sciences*, 280(1382):383–397, 1964.

[69] M. K. Tikhonravov, G. I. Sedlenek, and T. N. Trofimova, editors. *Works on Rocket Technology by E. K. Tsiolkovsky*. Publishing House of the Defense Ministry, Moscow, 1947. Translated from the 1947 Russian text by NASA as NASA TT F-243, 1965.

[70] Makoto Ue, Masayuki Takeda, Takako Takahashi, and Masahiro Takehara. Ionic liquids with low melting points and their application to double-layer capacitor electrolytes. *Electrochemical and Solid-State Letters*, 5(6):A119–A121, 2002.

[71] Julie Xie, Michael D. Canonica, and Paulo C. Lozano. Fabrication of electrospray thrusters by sintering glass microspheres. In *49th AIAA/ASME/SAE/ASEE Joint Propulsion Conference*, pages AIAA–2013–3824, 2013.

[72] John K. Ziemer. Performance measurements using a sub-micronewton resolution thrust stand. In *27th International Electric Propulsion Conference*, pages IEPC–01–238, Pasadena, USA, 2001.